

Are deep-ocean-generated surface-wave microseisms observed on land?

Peter D. Bromirski,¹ Ralph A. Stephen,² and Peter Gerstoft¹

Received 23 January 2013; revised 22 June 2013; accepted 24 June 2013; published 25 July 2013.

[1] Recent studies attribute land double-frequency (DF) microseism observations to deep water generation. Here we show that near-coastal generation is generally the dominant source region. This determination is based on observations at land and ocean seismic stations, buoys, gravity-wave hindcasts, and on beamforming results from continental seismic arrays. Interactions between opposing ocean wave components generate a pressure excitation pulse at twice the ocean wave frequency that excites pseudo-Rayleigh (*pRg*) wave DF microseisms. *pRg* generated in shallow coastal waters have most of their energy in the solid Earth (“elastic” *pRg*) and are observed by land-based and seafloor seismometers as DF microseisms. *pRg* generated in the deep ocean have most of their energy in the ocean (“acoustic” *pRg*) and are continuously observed on the ocean bottom, but acoustic *pRg* does not efficiently transition onto continents. High-amplitude DF signals over the [0.2, 0.3] Hz band observed on the deep seafloor are uncorrelated with continental observations and are not clearly detectable at individual continental stations or by land seismic-array beamforming. Below 0.2 Hz, modeling and some observations suggest that some deep water-generated elastic *pRg* energy can reach continental stations, providing that losses from scattering and transition across the continental-shelf boundary to the shore are not substantial. However, most observations indicate that generally little deep-ocean-generated DF microseism energy reaches continental stations. Effectively, DF land observations are dominated by near-coastal wave activity.

Citation: Bromirski, P. D., R. A. Stephen, and P. Gerstoft (2013), Are deep-ocean-generated surface-wave microseisms observed on land?, *J. Geophys. Res. Solid Earth*, 118, 3610–3629, doi:10.1002/jgrb.50268.

1. Introduction

[2] Multiple storms often occur concurrently across the North Pacific. Cyclonic storm systems can result in high waves propagating in multiple directions, and waves from different storm systems regularly interact. The interaction of opposing wave components having nearly the same wave number produces a pressure excitation pulse at double the gravity-wave frequency (DF) that propagates to the seafloor, where it is converted into various phases, including acoustic-gravity waves [Ardhuin and Herbers, 2013; Cox and Jacobs, 1989], Rayleigh and Love surface waves [Latham and Sutton, 1966; Fukao *et al.*, 2010], sediment shear modes [Schreiner and Dorman, 1990], and compressional and shear body waves [Gerstoft *et al.*, 2008; Haubrich and McCamy, 1969; Zhang *et al.*, 2010].

[3] The wave-wave interaction mechanism that produces the DF pressure signal has been described in numerous studies

[e.g., Longuet-Higgins, 1950; Hasselmann, 1963]. The amplitude of the DF pressure excitation signal depends on the amplitude of the opposing wave components and the area over which the interaction occurs. Thus, intermediate amplitude opposing waves could produce higher amplitude pressure fluctuations than the interaction of very high with very low amplitude opposing components. Similarly, interactions of low-amplitude waves over a large area could produce higher DF pressure fluctuations than very high-amplitude waves interacting over a small area. Identification of microseism source areas is complicated because the spectral characteristics of the forcing function (ocean gravity waves) are not stationary in either time or location. The combination of added wind energy imparted to the waves over time, and/or dispersion and dissipation under propagation away from the wave generation region, further complicate source function characteristics.

[4] Numerous ocean bottom seismometer (OBS) studies have described seafloor DF signal variability [e.g., Bradner and Dodds, 1964; McCreery *et al.*, 1993; Babcock *et al.*, 1994]. High-amplitude DF signals observed on the seafloor in the deep ocean result from local wave activity associated with nearby storms [Babcock *et al.*, 1994; Bromirski *et al.*, 2005; Harmon *et al.*, 2007]. Additionally, a significant portion of longer-period DF energy observed on the deep seafloor at frequencies between 0.1 and 0.15 Hz is generated by wave activity along distant coastlines [Bromirski *et al.*, 2005]. The deep-ocean DF noise spectrum typically shows

Additional supporting information may be found in the online version of this article.

¹Scripps Institution of Oceanography, University of California, San Diego La Jolla, California, USA.

²Woods Hole Oceanographic Institution, Woods Hole, Massachusetts, USA.

Corresponding author: P. D. Bromirski, Scripps Institution of Oceanography, University of California, San Diego, La Jolla, CA 92093-0209, USA. (pbromirski@ucsd.edu)

©2013. American Geophysical Union. All Rights Reserved.
2169-9313/13/10.1002/jgrb.50268

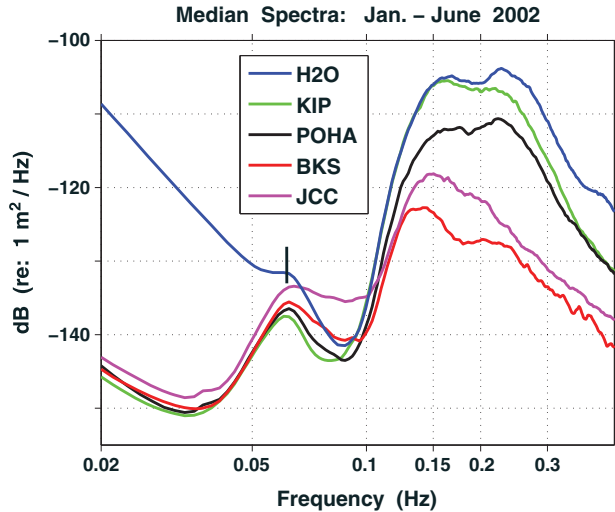


Figure 1. Median vertical component displacement spectra over the January–June 2002 time period at deep-ocean bottom site H2O, Hawaiian Island stations KIP (Oahu) and POHA (the Big Island of Hawaii), and near-coastal continental land stations BKS (Berkeley, CA) and JCC north of Cape Mendocino (Arcata, CA). See Figure 4 for locations. Note the absence of the 0.2–0.3 Hz peak at the continental stations. The rapid rise in H2O Guralp sensor levels (blue line) below about 0.065 Hz (indicated by the black vertical line) is tilt induced noise, a common feature of seafloor broadband spectra [Crawford *et al.*, 2006].

two peaks (H2O, Figure 1), with the higher-frequency peak between 0.2 and 0.3 Hz generated both locally and at relatively distant deep-ocean source regions [Babcock *et al.*, 1994; Bromirski *et al.*, 2005].

[5] Many analyses of land-based seismic-array data and individual seismic station data have identified coastal regions as the source area of DF Rayleigh microseisms [e.g., Bradner and Dodds, 1964; Haubrich and McCamy, 1969; Bromirski *et al.*, 1999; Bromirski, 2001; Bromirski and Duennebie, 2002; Rhie and Romanowicz, 2006; Tanimoto, 2007; Gerstoft and Tanimoto, 2007; Traer *et al.*, 2008; Zhang *et al.*, 2010; Traer *et al.*, 2012]. The DF peak at continental stations is generally at lower frequencies and with lower amplitude than at ocean bottom or deep-ocean island stations, with the oceanic spectral peak above 0.2 Hz absent at continental stations (Figure 1). Note that the DF spectral levels at island stations KIP and POHA are substantially higher than at continental stations BKS and JCC. A possible explanation for the island/continental differences is that energy losses from scattering and transitioning from deep water across the continent shelf boundary to the shore are substantial, while the Hawaiian Islands share common oceanic basaltic crust with deep-ocean source areas. The lower-frequency DF peak near 0.16 Hz has higher amplitude at KIP than at POHA as a result of generally higher wave energy at the northern Hawaiian Islands, which are nearer the dominant wave generation region in the North Pacific [Wang and Swail, 2001; Bromirski *et al.*, 2012]. Additionally, the Hawaiian Island stations detect microseism signals from all directions continuously, thus providing a relatively large source area for wave interactions by local short-period trade

wind-generated seas and contributing to the spectral peak above 0.2 Hz.

[6] That seismic noise levels observed by land-based stations are dominated by coastally generated DF microseisms associated with near-coastal wave activity has been demonstrated using array analyses [Haubrich and McCamy, 1969; Gerstoft and Tanimoto, 2007; Zhang *et al.*, 2010] and has been clearly shown by comparison of nearby simultaneous wave spectra and microseism spectra measurements [Haubrich *et al.*, 1963; Bromirski *et al.*, 1999; Bromirski and Duennebie, 2002]. In this paper, we consider near-coastal or shallow water as those coastal regions where water depth is less than one half the deep water gravity-wave wavelength, the depth at which ocean gravity waves begin to interact appreciably with the seafloor and thus where single-frequency (SF) microseisms are generated. Most of the energy in the DF spectrum is above 0.11–0.12 Hz (Figure 1), resulting from wave interactions between gravity waves having about 18 s periods (with wavelengths about 500 m) and shorter. We thus define water depths less than about 250 m as near-coastal, shallow water, covering most of the continental shelf and a portion of the continental slope. This definition of shallow water also demarcates the zone where the evanescent portion of the DF pressure spectrum [Cox and Jacobs, 1989; Bromirski and Duennebie, 2002] can provide an additional contribution to DF levels observed on land.

[7] DF microseisms observed at land seismic stations show a nearly one-to-one correspondence with nearby near-coastal wave activity [Bromirski *et al.*, 1999; Bromirski and Duennebie, 2002], indicating that DF microseism signals observed on land are dominated by coastal generation resulting from interactions between incoming and shore-reflected/scattered wave energy. While the preponderance of observational evidence indicates that deep water open-ocean generated DF microseisms do not propagate onto continents, some recent studies suggest that deep-ocean-generated DF microseisms in the North Pacific and North Atlantic are observed on land, including Cessaro [1994], Kedar *et al.* [2008], and most recently Obrebski *et al.* [2012]. The question is not whether high-amplitude DF pressure signals are generated in the deep ocean, which has been demonstrated by the various OBS studies previously mentioned, but whether these surface wave signals propagate efficiently from deep water onto land, i.e., without substantial energy losses.

[8] It is common in earthquake surface wave studies at frequencies below 0.1 Hz to ignore the water layer and to treat the seafloor as an elastic free surface [e.g., Zhang and Lay, 1995]. In this case, the surface wave problem is the same for oceanic crust as continental crust, and the surface waves are properly called Rayleigh waves (Rg) [Aki and Richards, 2002; Ewing *et al.*, 1957; Kennett, 2001]. At DF microseism frequencies from 0.1 to 0.4 Hz, the ocean can have significant thickness in terms of acoustic wavelengths. For pressure sources (as from wave-wave interaction), much of the DF energy propagates in the water column (not in the solid seafloor as is the case for Rg) [Latham and Sutton, 1966; Harmon *et al.*, 2007; Ardhuin and Herbers, 2013]. Following a long tradition, we refer to the surface waves under the oceans at DF microseism frequencies as “pseudo-Rayleigh waves” (pRg) [Roever *et al.*, 1959; Strick, 1959a, 1959b; Ewing *et al.*, 1957; Brekhovskikh, 1960; Biot, 1952; Cagniard, 1962; Scholte, 1948, 1949; Tolstoy, 1954; Bradley, 1994; Okal, 1988]. When the water-layer depth

approaches zero, pRg becomes indistinguishable from the free-surface Rayleigh wave (FSRW). For deep water and high frequencies, the pRg propagation speed diverges from the FSRW speed and approaches the water sound speed.

[9] The pRg energy distribution between the solid and fluid depends on the water depth where the wave interactions occur, with the proportion of pRg energy in the water layer increasing with water depth. When pRg has the characteristics of Rg, DF signals propagate as “elastic pRg.” When pRg has most of its energy in the water column, DF signals propagate as “acoustic pRg.” Since elastic pRg will transition to continental crust (i.e., to land seismometers) more readily than acoustic pRg, these distinctions are important in identifying potential DF microseism source areas.

[10] We present observations that indicate that near-coastal gravity-wave activity can explain the DF microseisms observed on land that have been attributed to deep-ocean sources during the observational period of the *Cessaro* [1994], *Kedar et al.* [2008], and *Obrebski et al.* [2012] studies. Gravity-wave dispersion and coincident primary microseism generation are used to help identify probable source areas, key factors not directly considered by the previous studies mentioned. The time-history relationships between wave climate variability and DF signals observed at land stations are investigated. Beamforming of array seismic data is used to determine the dominant source directions during the *Obrebski et al.* [2012] event. Model studies are used to describe the partition of energy between elastic and acoustic pRg as a function of both water-layer thickness and pressure excitation frequency.

[11] There are two methods to detect weak wave-generated signals using seismic arrays, cross correlation, and beamforming. Long-term noise cross correlation would show the potential for coherent propagation between two stations. Although *Lin et al.* [2006] found generally good coherence between widely separated stations using cross correlation at frequencies less than 0.1 Hz, scattering losses at higher frequencies identified by *Harmon et al.* [2007] could preclude adequate signal-to-noise (S/N) in the DF microseism band. To investigate the potential for DF signal coherence, we have attempted similar cross-correlation studies focused on time periods when very high-amplitude DF signals were detected on the deep seafloor and obtained negative results, suggesting that scattering losses may be significant at higher frequencies.

[12] Beamforming is needed to detect weak signals in noise. This method gives sufficient time resolution to detect localized microseism sources. Beamforming was employed extensively in attempts to detect localized deep-ocean microseism surface-wave sources [*Gerstoft et al.*, 2006, 2008; *Gerstoft and Tanimoto*, 2007; *Zhang et al.*, 2010; *Traer et al.*, 2012]. While deep water P-wave microseism source regions were identified, none of these investigations detected Rayleigh waves incident from the regions corresponding to P wave microseism back azimuths. Our conclusion from these studies is that coastal microseisms are dominant, which we justify here with detailed analyses of a variety of observations.

[13] In this study, wave climate relationships with DF microseism variability are established using a combination of (i) global wave model significant wave height (*Hs*) hindcasts (WAVEWATCH III ver 3.14, WW3; *Tolman* [2009]) forced by National Oceanic and Atmospheric Administration (NOAA) National Center for Environmental

Prediction (NCEP) reanalysis project near-surface winds (NRA-1; *Kalnay et al.* [1996]) for pre-1992 comparisons, (ii) NOAA buoy wave spectra, and (iii) hindcast WW3 *Hs* since 1992 obtained from <http://polar.ncep.noaa.gov>.

2. Source Area Identification Factors

[14] SF (also called “primary”) microseisms are generated only in shallow water at gravity-wave frequencies by direct-pressure oscillations forced by waves impacting the nearshore sloping seafloor [*Hasselmann*, 1963]. Thus, because SF microseisms can be generated only in shallow water, the concurrent observation of SF and associated DF microseisms having similar time histories indicates coincident nearshore generation of both of these signals. In general, it is unlikely that SF and DF microseisms with the same temporal behavior and relative power characteristics, consistent with dispersed gravity-wave arrivals at coasts, would occur in different locations.

[15] An important discriminator of DF generation location is gravity-wave dispersion. While spectral levels over DF bands can be useful for identifying signals from common events at widely separated stations [*Bromirski*, 2001; *Bromirski et al.*, 2005; *Kedar et al.*, 2008; *Obrebski et al.*, 2012], differences in spectral patterns and their dispersion at multiple stations are useful for identifying progressive changes in DF generation location associated with swell propagation [*Bromirski and Duennebieer*, 2002], particularly at coastal continental stations.

[16] Recent significant advances in wave interaction DF modeling efforts by *Ardhuin et al.* [2011] have resulted from improved modeled wave directional spectral estimates and also include coastal reflection. These improvements have spurred attempts to identify deep-ocean sources of DF microseisms observed on continents. Along coasts, shore reflection plays a critical role in providing the opposing wavefield, particularly at wave periods greater than 12 s. Wave reflection from coasts is complicated and depends on several factors, including deep water approach angle, wave transformation from deep water to the shore (shallow water bathymetry), wave amplitude and frequency, and beach slope and composition [*Elgar et al.*, 1994]. Model DF estimates that incorporate wave reflection from coastlines generally track observations [*Ardhuin et al.*, 2011; *Bromirski et al.*, 1999], although it is unclear to what degree discrepancies between modeled DF amplitudes and seismic observations result from incorrect estimates of wave reflection, contributions from nonlocal sources, or DF propagation issues. Potentially, DF levels observed on land are dominated by wave interaction nearshore in shallow water where reflected (opposing) amplitudes may be greater, and where DF energy generated produces mostly elastic pRg that easily propagates inland.

3. Identification of Deep-Ocean DF Source Locations

[17] Deep-ocean sources of DF microseisms observed by continental seismic stations have been determined for a few isolated cases, both by array studies [*Cessaro*, 1994] and hindcast wave-wave interaction modeling to explain seismometer observations [*Kedar et al.*, 2008; *Ardhuin et al.*, 2011; *Obrebski et al.*, 2012]. Here we investigate wave conditions with WW3 hindcast *Hs* (see Supplement S1 for WW3

Hs time-history validation) and (when available) buoy wave spectra and contemporaneous vertical seismometer observations, to examine the time histories of spectral variability during key events, with our primary focus on the exceptional event identified by *Obrebski et al.* [2012], discussed in detail in section 3.1. Because band-limited *Hs* over the dominant portion of the ocean wave spectrum and the corresponding DF microseism spectrum are well correlated [*Bromirski et al.*, 1999], model *Hs* spatial patterns are a satisfactory proxy for estimating the potential for DF-generating wave interactions. However, it is important to note that there can be considerable uncertainty in both regional and remote wind fields that force wave models, particularly for small short-duration storms.

3.1. Midlatitude Eastern North Pacific

[18] Recently, *Obrebski et al.* [2012] identified a strong DF event observed at several continental and island seismic stations during 29 May to 1 June 2002. They attributed these DF signals to deep-ocean wave interactions between southward propagating swell and northward propagating waves from Hurricane Alma, which reached peak wind speeds on 30 May, 0600–1200 h near 16°N, 245°E (Figure 2a). The spatiotemporal variability of eastern North Pacific *Hs*, gravity-wave spectra, and microseism spectra during this exceptional event provide an opportunity to investigate factors that both help constrain potential DF generation locations and their ambiguity.

[19] Important for confirming a model-estimated deep-ocean DF source location observed by continental and island stations is the time history of spectral variability over a sufficiently wide frequency band that encompasses most of the wave energy for that event. The strong extratropical cyclone (ETC) that forced the dominant wavefield spanned a large area over the eastern North Pacific (Figure 2a), producing long-period broad-wavefront swell propagating east-southeastward along the Pacific coast of North America, generating SF and DF microseisms (Figures 2c–2h). The characteristics of this wave event were such that a long stretch of coast was nearly simultaneously illuminated by relatively high-amplitude (about 4 m *Hs*) waves having very similar wave spectra (Figure 3). The large coastal region of wave-wave interaction contributed to the high-amplitude DF event observed. Differences between the wave and associated DF spectra at progressively southward locations are explained by small differences in wavefront propagation direction and gravity-wave dispersion, most clearly evidenced by the time delay of the onset of high spectral levels and elongation of the peak DF energy band over time (compare Figures 2d and 2h). The higher DF levels along the Baja, Mexico coast at NE74 (Figure 2g) likely result from elevated opposing wave energy due to the geometry of Bahia de Sebastian Vizcaino, emphasizing both the importance of coastal reflection for opposing wave components and the dominance of near-coastal generation of DF microseisms for this event. The wave spectrum at buoy 46001 near Alaska (Figure 3a) is similar to the other buoys, showing the broad spatial extent of waves from this storm. The lower wave energy at 46001 is consistent with the lower DF energy at Alaskan seismic station KDAK shown by *Obrebski et al.* [2012], and also consistent with DF levels at near-coastal

seismic stations being dominated by local waves [*Bromirski and Duennebieer*, 2002] (compare Figures 2 and 3).

[20] SF microseisms in the [0.05, 0.08] Hz band have approximately the same time history (and associated dispersion trends) as the DF signals along the California coast (Figures 2d–2f). The slope of the gravity-wave spectra dispersion trends (Figures 3c–3f; white lines) is consistent with the DF spectral energy trends in Figure 2. This consistent pattern of associated spectral viability for both SF and DF microseisms is indicative of coastal DF generation.

[21] DF energy preceding the swell arrival at more southern land seismic stations (Figures 2g and 2h, the spectral region between the black and white lines) likely results from Rayleigh wave arrivals from DF generation along the coast at more northern locations. Relative-amplitude comparisons suggest that DF energy preceding the initial DF signal from this event (i.e., preceding the black lines in Figure 2) results from interaction of waves from Hurricane Alma along the Baja, Mexico coast, on 28–29 May. These signals propagate to the other stations as Rayleigh waves, with the more southern coastal source region evidenced by their general decrease in amplitude with distance northward. It should be noted that the somewhat higher frequency of these DF signals is more consistent with wave periods associated with small, short-duration hurricanes such as Alma than the 20 s period waves needed to produce the 0.1 Hz DF microseisms during 30 May in Figure 2 and the wave energy below 0.06 Hz in Figure 3. Note that the peak in the ocean wave spectrum at southernmost buoy 46047 (Figure 3f) trails the more northern buoys, indicative of north-to-south swell propagation.

3.1.1. Variable DF Source Directions From Beamforming

[22] The beamforming methodology of *Gerstoft and Tanimoto* [2007] was applied to seismic-array data from both Southern California Seismic Network (SCSN) and the Northern California Earthquake Data Center (NCEDC) BK networks (Figure 4a) to obtain estimates of the dominant DF microseism source directions during the *Obrebski et al.* [2012] wave event. Beamforming of vertical component data from these arrays was performed over three frequency bands in an effort to determine whether multiple DF source regions could be identified, potentially associated with either changes in the gravity wavefield resulting from dispersion or the presence of waves from Hurricane Alma. The less dense BK network shows a relatively consistent dominant source direction at about 265° azimuth during 30–31 May, consistent with DF levels being dominated by wave activity at the nearby coast [*Bromirski and Duennebieer*, 2002]. There is no clear indication of significant DF energy arriving from the *Obrebski et al.* [2012] deep-ocean source locations. The low density and spatial configuration of the BK network did not allow investigation of source directions of DF signals above 0.115 Hz and caused the beam-power artifacts near azimuths 175° and 300°.

[23] The higher density SCSN network allows a more thorough investigation of the dominant beam-power directions during 27 May to 1 June, showing a considerably different pattern of DF source azimuths for different frequency bands. At lower frequencies, SCSN shows a general north-to-south temporal progression in the maximum beam-power azimuths (Figure 4d), dominated initially at more northern locations where wave intensity is greater (compare with Figures 3b and 3e). The beam-power time history is consistent with

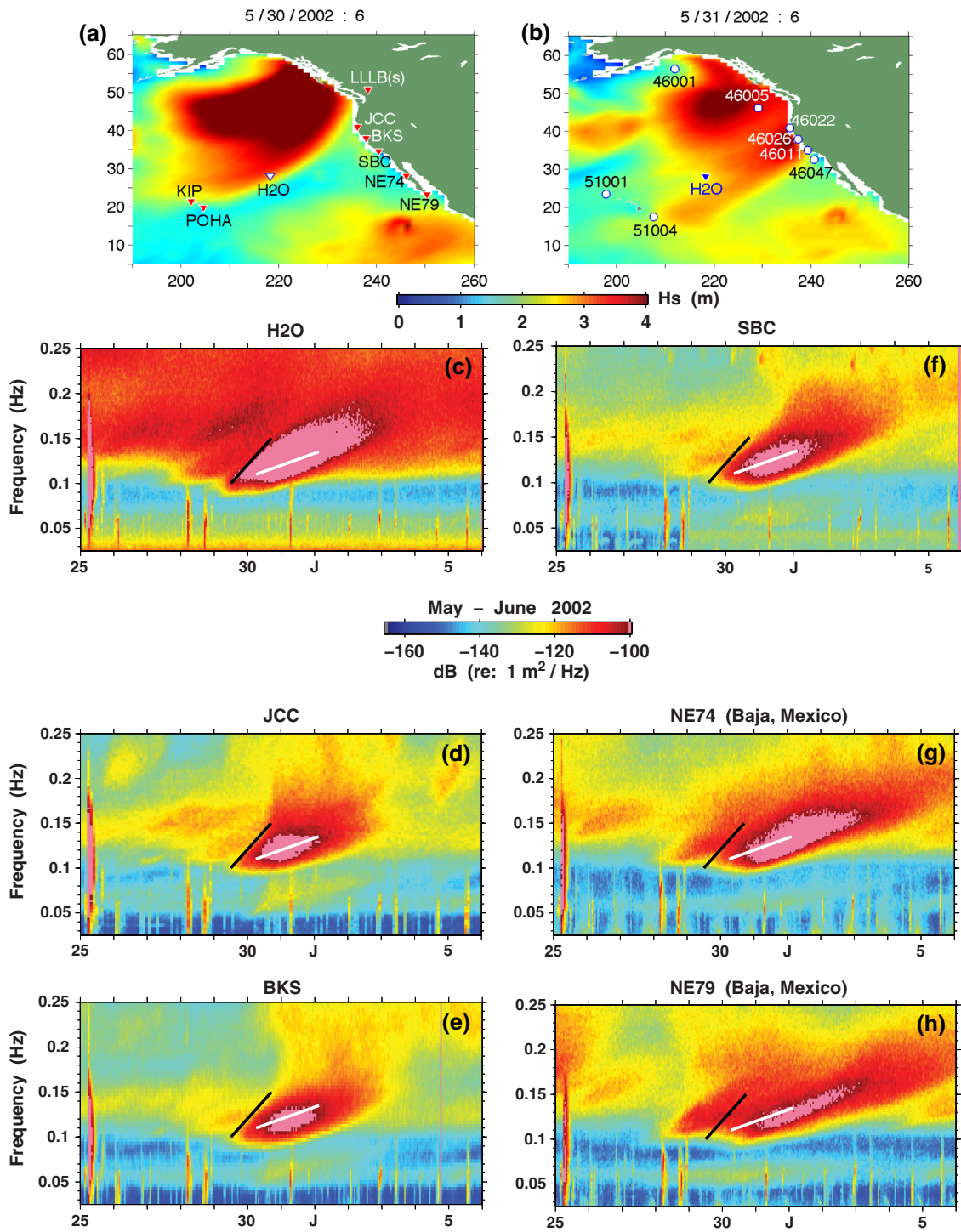


Figure 2. Near-coastal DF microseism generation associated with north-to-south swell propagation. (a) WW3 H_s snapshot at 30 May 2002 0600 h, showing locations of seismometer stations in Figures 2c–2h. (b) WW3 snapshot at 31 May 2002 0600 h, showing the change in wave height resulting from southward propagation of the swell, and the locations of NOAA buoys compared in Figure 5. (c)–(h) Spectrograms over the 25 May to 5 June time period spanning the southward propagating swell and Hurricane Alma (southeast corner in Figures 2a and 2b) storm events. Dispersion trend lines are relative to JCC (d), and are common in Figures 2c–2h for reference. The scale range applies to all stations.

coincident source locations distributed along much of the coast, e.g., on 30 May 00 h, but with the general temporal trend in the dominant beam-power azimuths also consistent with north-to-south swell propagation along the coast.

[24] The apparent multiple-azimuth strong beam-power distribution on 29–30 May in Figure 4e (the band used by *Obrebski et al.* [2012] in Figure 1) is consistent with nearly simultaneous illumination of a long stretch of coastline by

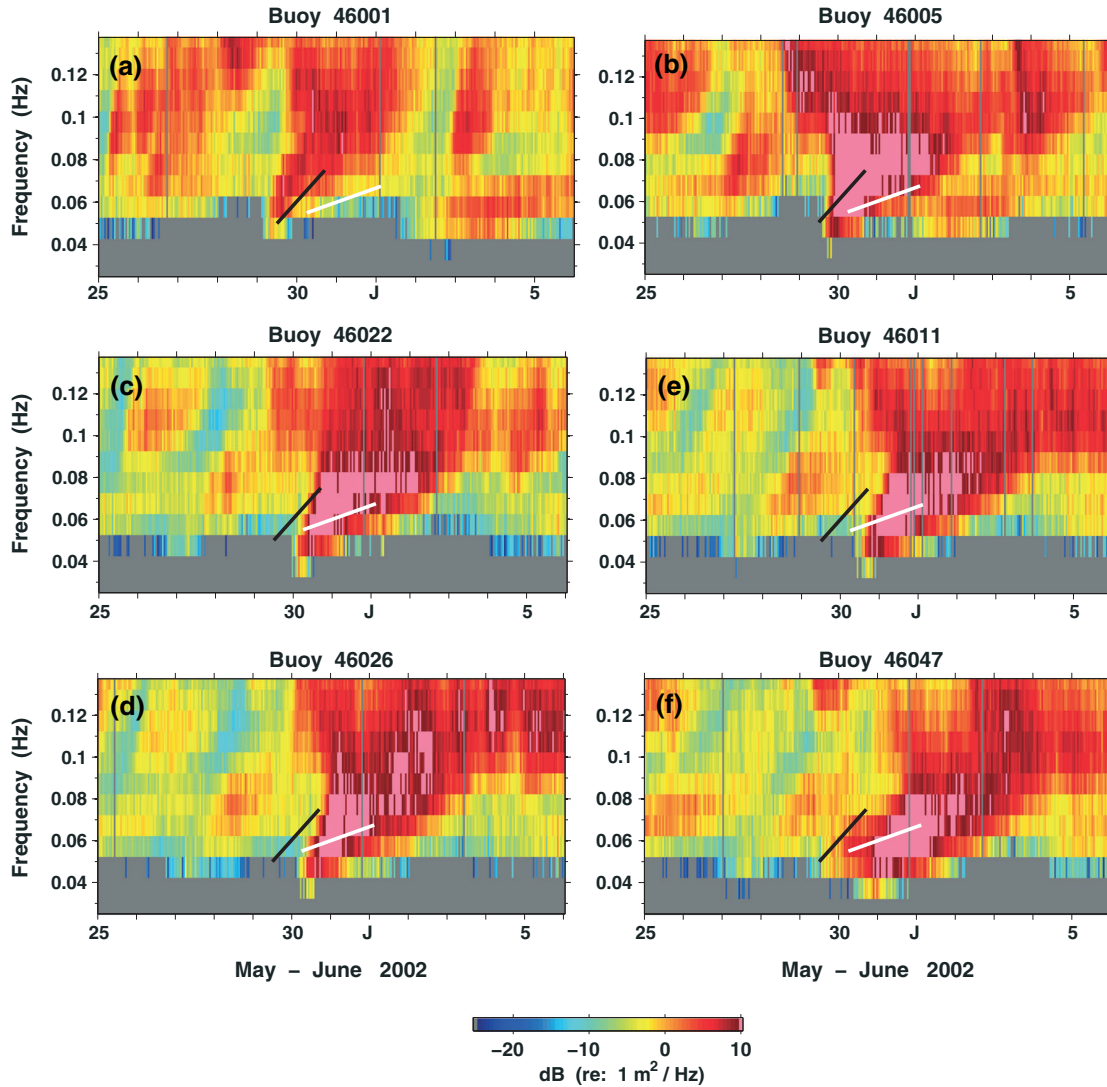


Figure 3. Wave spectra from NOAA buoy measurements showing southward propagation of the 29 May to 1 June swell event along the Pacific coast of North America. The locations of NOAA buoys where the wave spectra in Figures 3a–3f were measured are shown in Figure 2b. The spectral amplitude scale applies to all. Temporal locations of dispersion trends (black and white lines) are common with those in Figure 2, but have half the DF slopes.

swell, producing high-amplitude DF signals at multiple coastal locations (Figure 2), and also north-to-south swell propagation. The increased beam power on 31 May at less than 225° azimuth (Figure 4e) likely results from near-coastal interactions of southward propagating waves along the Baja coast, where coastal wave activity intensifies as swell from the north escapes the shadowing effects of Pt. Conception [Schulte-Pelkum *et al.*, 2004]. The impact of gravity waves from Hurricane Alma along the Baja and California coasts is manifested by the beam-power concentration on 27–29 May between azimuths $155\text{--}215^\circ$ (Figures 4e and 4f). The absence of signals from Alma in Figure 4d indicates that this relatively small short-duration hurricane produced little wave energy in the associated gravity-wave band.

[25] The differences in beam-power distribution between the bands in Figures 4e and 4f, i.e., increasing energy at shorter periods at later times at more southerly locations, are consistent with energy patterns associated with the

north-to-south gravity-wave dispersion in Figures 2 and 3. Thus, the SCSN beam power has some power in the direction of the *Obrebski et al.* [2012] source locations, but the progressive changes in the spectral energy distribution (and the presence of associated SF microseisms) are consistent with wave interaction associated with dispersed ocean waves hitting the coast. We also note that the polarization analysis in *Obrebski et al.* appears to be consistent with progressively southward coastal microseism generation as the swell propagates southward along the coast.

3.2. Deep Seafloor-Continental-Island-Wave Spectra Comparisons

[26] Critical for confirming a deep-ocean source location for the land DF observations is their relationship with DF signals observed at mid-ocean station H2O (Figure 2c). Based on the spectral characteristics, we define the long-period double-frequency (LPDF) [0.11, 0.14] Hz band to span most of

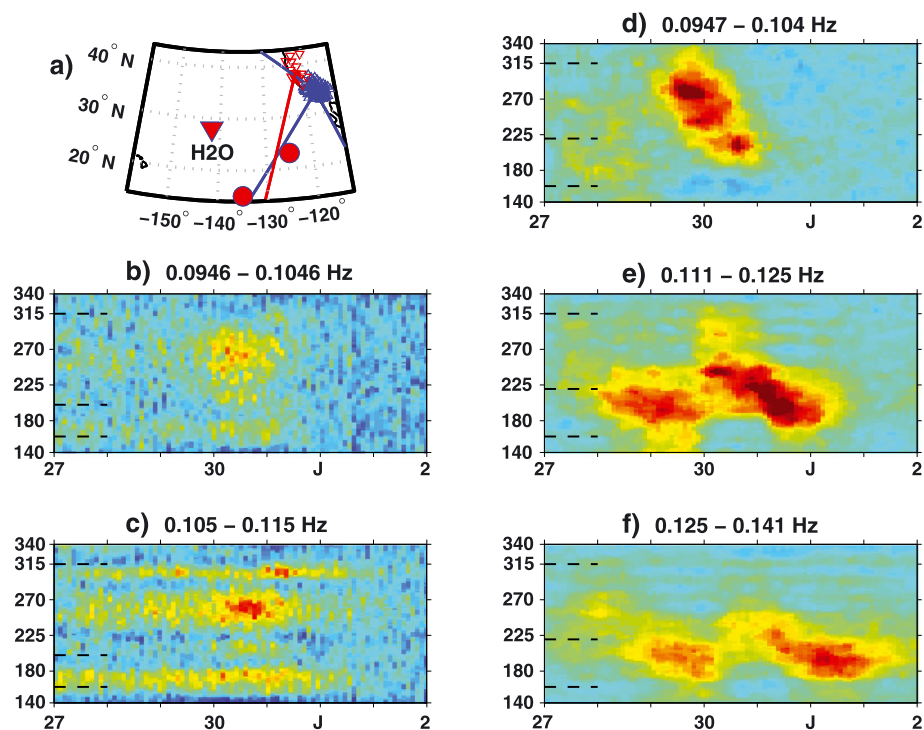


Figure 4. (a) SCSN (blue triangle cluster) and Northern California BK Network (red triangles) station locations. Beamformer power versus azimuth over 27 May to 1 June determined from vertical component seismic data at (b–c) the BK network, and (d–f) the SCSN network stations over the frequency bands indicated (linear power scale, blue (low) to dark red (high)). Dashed lines in Figures 4b–4f show azimuths corresponding to potential source directions (blue lines) in Figure 4a, north (315°) and south (160°) along the coast, and toward estimated *Obrebski et al.* [2012, Figure 3] deep-ocean source locations (red circles) at 220° from the SCSN network and at 200° (red line) from the BK network. Beamformer responses were median filtered to emphasize the dominant beam-power directions. Horizontal bands in Figures 4b and 4c are processing artifacts resulting from the BK network station distribution.

the dominant spectral band shown in Figure 2, in contrast to the narrower $[0.111, 0.125]$ Hz band used by *Obrebski et al.* For other events, the LPDF band extends to both higher and lower frequencies, depending on the wave spectral content. Wavefronts from the ETC reached H2O about a day prior to the *Obrebski et al.* modeling focus (their Figure 2) and prior to swell arrival along the California coastline (Figure 2a). In fact, some DF energy was likely generated north of H2O, evidenced by the elevated DF energy levels at H2O prior to 30 May (Figures 2c and 2a). Root mean square (RMS) levels of the wave spectra (Figure 5b), that correspond to the seismic LPDF band, show wave energy levels at more northern buoy 46005 rising in consort with DF levels at H2O (compare Figures 5a and 5b), consistent with some DF energy arriving from more northern deep-ocean wave activity.

[27] Although long-period gravity waves from both the extratropical storm and Hurricane Alma could have interacted south of H2O on 30 May, it seems unlikely that the seismic trends would then display the same pattern of dispersion associated with southeastward travelling swell. The slopes of these swell-associated dispersion trends are masked by signals generated at multiple coastal locations, and because the storm-generated swell approach angle was from a westward direction, the apparent dispersion is similar along much of the coast. However, the characteristics of the DF

spectral trend patterns change with station distance north-to-south from the extratropical wave generation region (Figure 2), with the onset of the spectral peak progressively delayed and extended to higher frequencies southward (note the delay between the elevated spectral levels and the black reference line from JCC). These lags are not consistent with northward travelling waves from Alma. Furthermore, the presence of SF microseisms indicates near-coastal generation.

[28] Coastal buoy RMS levels consistently lag H2O, having time histories similar to DF observations at nearby near-coastal continental seismic stations, reflecting the variability shown in Figure 2. Note the good agreement between RMS temporal variability at Baja station NE74 and southernmost buoy 46047, i.e., both lag their more northern counterparts. Very similar RMS spectral levels are observed for coastal buoys in Figure 5b, consistent with high-amplitude DF microseism generation resulting from wave interactions associated with a nearly simultaneous illumination of a long stretch of coast by swell with similar spectral characteristics. Differences between buoy spectra are affected by their exposure to wave arrivals, local winds, and bathymetry.

[29] As indicated by WW3 snapshots in Figures 2a and 2b, wavefronts associated with the ETC event extend to the Hawaiian Islands, lagging H2O, but approximately coincident with swell arrivals at the northern California coast. LPDF

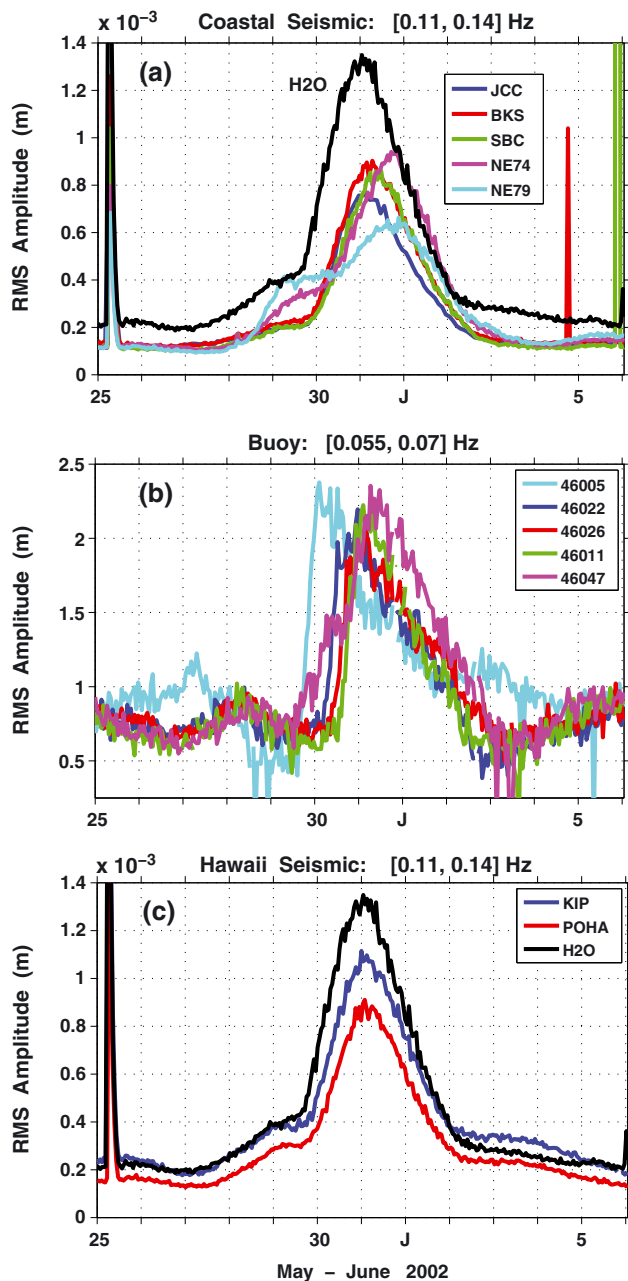


Figure 5. Root mean square (RMS) amplitudes of hourly averaged vertical component displacement spectral estimates from land-based seismic stations in the LPDF [0.11, 0.14] Hz band at (a) coastal stations, (b) from buoy wave spectra near the seismic stations in the [0.055, 0.070] Hz band, and (c) Hawaiian island stations KIP on Oahu and POHA on the Big Island of Hawaii. RMS amplitudes at deep-ocean bottom site H2O are added for comparison with the land-based stations. A magnitude 6.3 Aleutian Island earthquake signal produces the amplitude spike on 25 May 2002 that is common to all stations. Smaller earthquakes occurred near BKS on 4 June and near SBC on 5 June.

RMS levels at Hawaiian Island stations KIP and POHA (Figure 5c) show LPDF variability that is consistent with swell arrivals from the north, i.e., elevated levels at more northern KIP precede POHA, with higher levels at KIP consistent with more energetic wave activity farther north.

3.3. North Pacific

[30] The Large Aperture Seismic Array (LASA) in Montana during the 1960s and 1970s provided an opportunity to identify microseism source regions. Initial studies with LASA showed that fundamental and higher mode DF microseism Rayleigh waves were generated only in coastal regions [Haubrich and McCamy, 1969; Lacoss et al., 1969]. Cessaro [1994] augmented LASA with the Alaskan Long Period Array (ALPA) and the more distant Norwegian Seismic Array (NSA), identifying DF source regions using three-array triangulation and projections of half-beam-power directions. Attenuation of DF microseism Rayleigh waves can be appreciable over teleseismic distances, reducing the utility of NSA for DF source region localizations in the North Pacific. Cessaro's localizations appeared to correlate well with storm intensities from the Mariners Weather Log for 1973. However, estimating gravity-wave heights and characteristics are problematic using weather logs alone. Here we have the advantage of having WW3 hindcast H_s data (that were unavailable to Cessaro) to investigate gravity-wave conditions, which allows us to reinterpret his results. The H_s hindcast data show acceptable correlations with more recent NOAA buoy H_s data over the eastern North Pacific (see Supplement S2 for WW3 H_s time-history validation), implying that they give a reasonably reliable representation of gravity-wave conditions during 1973.

[31] Snapshots of WW3 H_s over the eastern North Pacific (Figure 6) show an extreme wave event along the south coast of Alaska during two time periods from Figure 4 of Cessaro [1994]. Because the nearest coastline dominates DF microseism levels [Bromirski and Duennebieer, 2002], in both instances, LASA and ALPA would be expected to point toward the suggested source regions determined by Cessaro from the intersection of the array beam-power directions. However, the WW3 H_s snapshots suggest that source regions were more likely their respective nearest coastlines. This is particularly evident in Figure 6b, where Cessaro identified two source regions for the same time interval that are consistent with the arrays pointing toward their respective nearest coastlines where wave activity was high. While the LASA and ALPA data are not available, coastal source areas for these two time intervals seem more likely since C1 in Figure 6a and the southern C11 in Figure 6b both occur in low H_s regions, where significant wave interaction is unlikely.

[32] Recent studies using the larger SCSN array (compared with arrays used by Cessaro [1994]) have searched for mid-ocean source locations of DF surface wave microseisms along the Pacific coast of North America [Gerstoft and Tanimoto, 2007] and under extreme tropical cyclones [Gerstoft et al., 2006; Zhang et al., 2010]. Gerstoft and Tanimoto determined only near-coastal source areas for a full year of SCSN data, while Zhang et al. found only compressional body wave microseisms emanating from the mid-ocean region near a western Pacific typhoon. These array studies are consistent with the hypothesis that only near-coastally generated DF microseisms are observed on continents.

3.4. North Atlantic

[33] Babcock et al. [1994] observed DF microseisms on the deep-ocean seafloor (depth about 3400 m) off the coast of North Carolina that correlated well with time histories of

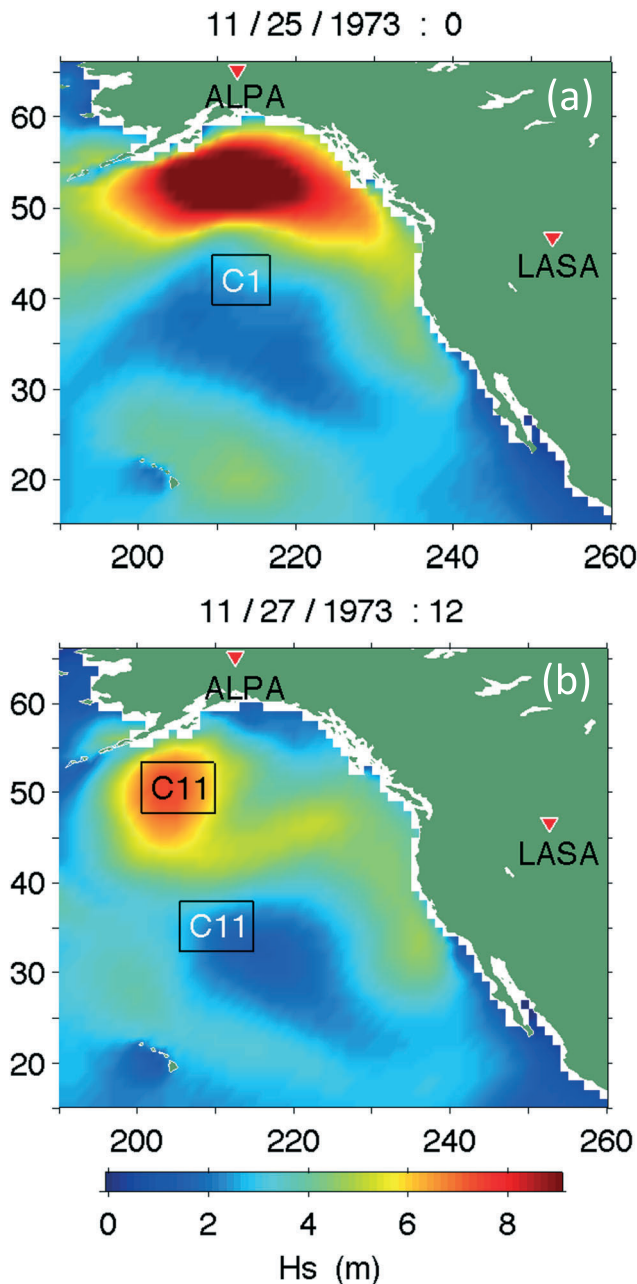


Figure 6. Wave model significant wave height (H_s) snapshots over the eastern North Pacific showing the temporal evolution of the wave climate during November 1973, also showing the locations of the LASA and ALPA arrays. Also shown are locations of DF microseism source areas determined by Cessaro [1994], C1 in Figure 6a and C11 in Figure 6b, with locations estimated from Figure 6 of Cessaro [1994].

local overhead wave activity during high-amplitude wave events, indicating that high-amplitude DF microseisms are commonly generated in deep water in the western North Atlantic under individual storms. Apparently, there is generally sufficient wave energy at opposing frequencies to always generate DF pressure signals under developed or developing seas. Additionally, Babcock *et al.* found that teleseismic SF and DF peaks with the same time history occurred simultaneously, suggesting a common near-coastal generation

location for those signals. As observed in the mid-Pacific at H2O (Figure 1), the western North Atlantic DF spectral peak is between 0.16 and 0.3 Hz, higher than at land stations [Babcock *et al.*, 1994; their Figure 10].

[34] That deep-ocean-generated DF microseisms are not observed on continents is also demonstrated by seismic and wave observations during the October 1991 Halloween Storm *Bromirski* [2001]. During that time period, northward-propagating high-amplitude waves from northward-travelling Hurricane Grace must have occurred, providing significant opposing wave energy to the southward-propagating waves from the Halloween Storm observed by NOAA buoys off the U.S. East Coast. The interaction of waves from these two storm systems must have produced high-amplitude DF pressure fluctuations in the deep ocean. However, strong DF microseisms were observed at continental seismic stations only when waves from these storms reached the coast.

[35] Kedar *et al.* [2008] modeled wave interactions southeast of Greenland during November 2003 using WW3 wave spectral estimates and attributed land DF microseism observations to mid-ocean wave activity. Their model did not include, however, coastal wave interactions between incident and coastally reflected wave components. Here we investigate the possibility that coastal wave activity was responsible for the DF signals observed at continental stations at that time. The WW3 H_s distribution over the North Atlantic during 31 October to 2 November at 00 h of each day (Figures 7a–7c) shows the evolution of the wave climate with spectral levels at three widely distributed land seismic stations (Figures 7d–7f) spanning that time period (see Supplement S3 for WW3 H_s time history). We note that the H_s pattern at 2 November 00 h (Figure 7c) most closely corresponds to Figure 5 of Kedar *et al.* (and not 1 November 00 h). At that time (2 November 00 h), relatively low DF levels were observed at PAB and SCHQ, consistent with declining wave energy along coasts near those stations (Figures 7b and 7c). Figure 7c indicates that, although high gravity-wave amplitudes from the two storm systems suggest high-amplitude DF fluctuations were likely produced over the deep ocean (as shown by Babcock *et al.* [1994]), the DF levels at PAB and SCHQ were decreasing over 2 November (Figures 7d and 7e), consistent with the hindcast H_s spatial patterns. Thus, land DF levels are generally not well-correlated with deep-ocean wave activity and associated deep-ocean DF microseism levels. Furthermore, the similar amplitudes for most of the earthquake Rayleigh wave (Rg) arrivals (Figures 7d–7f) at each of the stations indicate consistent propagation characteristics for Rg from earthquakes, in contrast to the large differences in ocean-generated pRg patterns. This suggests that either pRg levels observed on land are dominated by local generation, and/or that basin geology has a greater effect on pRg propagation than on Rg propagation.

[36] The spectral pattern at seismic station PAB (Figure 7d) shows characteristic patterns of SF and DF microseisms generated by dispersed swell arrivals impacting the Iberian coast of Spain, with the relatively low microseism amplitudes resulting from propagation losses due to its distance from the coast [Bromirski and Duennebier, 2002]. The spectral pattern at SCHQ (Figure 7e) is typical for developing seas, with the wave energy peak shifting to progressively lower frequencies over time from 31 October 1200 h to 1 November 00 h as the intensifying storm-driven wave field develops. The SF also shows a corresponding downward trend in peak frequency, indicating

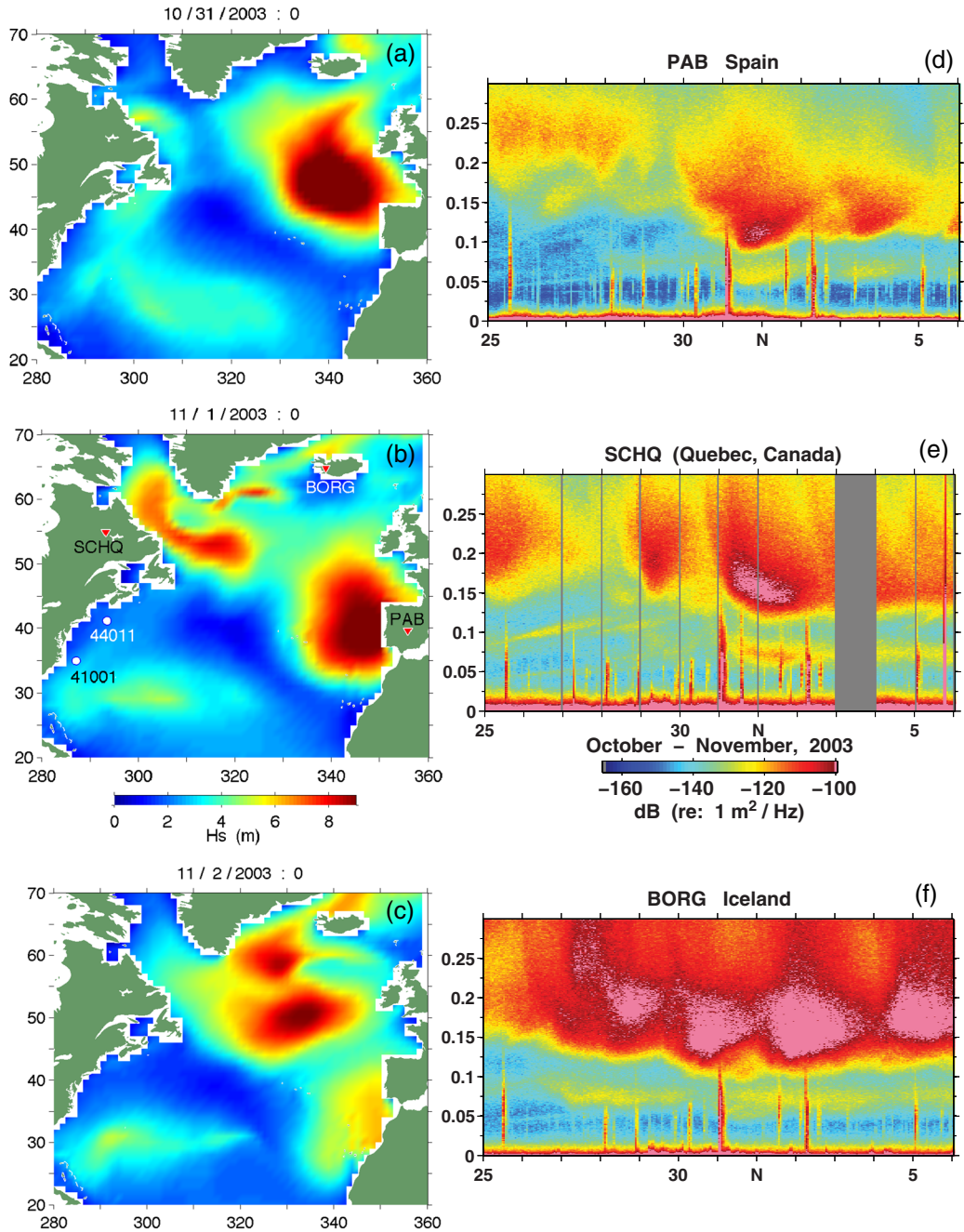


Figure 7. Wave model significant wave height (H_s) snapshots over the North Atlantic for (a) 31 October, (b) 1 November, and (c) 2 November 2003. Scaling in Figure 7b is common to Figures 7a and 7c. Vertical component seismic spectral variability over the 25 October to 5 November time period at land-based seismic stations in (d) Spain (PAB), (e) Quebec, Canada (SCHQ, data on 3 November not available), and (f) Iceland (BORG), with their locations shown in Figure 7b. SF (0.05–0.1 Hz) and DF (0.1–0.2 Hz) microseisms have similar time histories, indicating that both are generated at the same time and place, i.e., at nearshore locations. Short-duration high-amplitude transients at frequencies < 0.1 Hz are Rayleigh wave (Rg) earthquake arrivals.

near-coastal generation of both signals. Together, the SF and DF patterns are consistent with coastal reflection providing the opposing wave energy for near-coastal generation of the DF microseisms observed at SCHQ. Thus, deep-ocean sources are not necessary to explain the variability of land DF microseism levels surrounding the North Atlantic.

3.4.1. Implications From Other North Atlantic Observations

[37] Interestingly, inversion for source distance and generation time of the gravity waves causing the dispersed SF and DF (in the [0.09, 0.11] Hz band) linear trend patterns at SCHQ on 25–29 October [Haubrich *et al.*, 1963] indicates that

the generating swell originated 11,000 km from its coastal interaction, placing the wave generation region in the Southern Hemisphere on 18 October 2003. The much lower levels of these signals at PAB (barely discernable) suggest SF and DF microseism generation along either the Atlantic or Pacific coast of North America. Examination of the WW3 *Hs* field during 18 October (Supplement Figure S4) shows a strong wave event in the Southern Ocean southeast of New Zealand. Likely, swell from this event generated the microseisms along the Pacific coast, which propagated across North America to SCHQ as Rayleigh waves.

[38] Swell may travel long distances before interacting with the coast [Haubruch *et al.*, 1963; Bromirski and Duennebie, 2002]. Since the *Hs* maps depend mostly on regional winds, low-amplitude swell events propagating from distant storms will not appear on the *Hs* maps nor be detectable by ocean surface buoys. Consequently, there are coastal wave interactions that are not indicated by the *Hs* maps. The strong dispersion event at SCHQ is not observed at PAB and BORG (and the spectrograms are in general quite different), indicating that nearby near-coastal wave activity produces the DF signals. Thus, seismic stations separated by oceanic paths generally have different microseism patterns, and the microseism time history will be independent because they result from local-to-regional near-coastal wave activity.

[39] The spectral levels at BORG (Figure 7f) are similar to island stations KIP and POHA (Figure 1), i.e., the DF spectral peak is at a significantly higher frequency than at PAB and SCHQ. Note that the spectral peaks at PAB and SCHQ near 1 November 00 h correspond to a relative minimum at BORG, when wave activity along the southern coast of Iceland was low. These distinctly different spectral time histories are consistent with the poor correlation of *Rg* and *Lg* microseisms expected between stations separated by oceanic paths [Kennett, 1986; Cao and Muirhead, 1993; Zhang and Lay, 1995]. The increase in DF levels at BORG on 1 November is consistent with heightening wave activity along Iceland's north coast shown in Figures 7b and 7c. The pattern of DF spectral variability at BORG is considerably different than at the continental stations, reflecting both BORG's proximity to the Icelandic coast and coastal wave climate variability along its multiple, irregular, steep, shoreline exposures.

4. Relationships Between Long-Term Gravity-Wave-Induced Signal Variability at Mid-Ocean Bottom and Land Stations

[40] Although there is no question that DF pressure fluctuations commonly occur over all ocean regions, there is no unambiguous evidence that these generate Rayleigh waves that are observed on land. It seems likely that if deep-ocean-generated DF microseisms were observed on land, such observations would occur more often, i.e., rare, infrequent combinations of storm events would not be essential for their detection. We next investigate long-term relationships between mid-ocean wave-induced seafloor signals and those recorded on land, both on continents and on islands, over 6 month time periods.

4.1. Mid-Ocean Versus Continental Wave-Generated Signal Variability

[41] The time histories of LPDF levels at H2O and BKS are necessarily similar because storm wave events are

generally common to both locations, either nearly simultaneously (Figures 2a and 2b) or delayed by west-to-east storm and swell propagation times. Comparing RMS spectral levels between H2O and BKS in the SF and LPDF bands (Figures 8c and 8d), similar time variability is observed, clearer and more pronounced for the higher amplitude [0.11, 0.14] Hz LPDF band. Higher amplitudes at H2O in the LPDF band may result from ocean bottom site characteristics, ocean resonance amplification, and/or nonlocally deep-ocean-generated seismo-acoustic energy. Amplitudes in the SF band at H2O are strongly affected by tilt noise (see Figure 1). The time series in Figures 8c and 8d are well correlated (Figure 8f), suggesting that the SF and LPDF signals are common to both stations. The much lower SF amplitudes, having low S/N ratios, together with tilt contamination at H2O, explain the somewhat lower R^2 values. SF signals generated along the U.S. West Coast closest to H2O likely provide the dominant contribution, with the Hawaiian Islands another potentially strong SF source region. The close to zero lag between the hourly SF RMS levels is attributable to Rayleigh wave phase speeds.

[42] The higher amplitude LPDF signals have better S/N and are not significantly affected by instrument tilt, resulting in significantly higher correlation between the stations. Interestingly, the signals at H2O lead BKS. This can be explained by a combination of LPDF microseisms being generated at locations along the West Coast north of BKS (Figure 2), and also in the open ocean north (or south) of H2O, that propagate more efficiently to H2O. Near-coastal LPDF microseism generation from later-arriving swell reaching the coast nearest BKS provides the dominant contribution to signal levels at BKS [Bromirski and Duennebie, 2002], resulting in the dominant BKS DF signals lagging H2O. The broadness of the LPDF correlation function is likely due to DF levels from larger and/or nonlocal source areas. That H2O leads BKS also suggests that LPDF signals generated in the open ocean south of H2O are generally less significant. The 5 h lag difference is inconsistent with a common source area. The large difference in spectral levels between H2O and BKS (>30 dB at the ~ 0.225 Hz spectral peak, Figure 1) indicates inefficient propagation from the deep ocean to continents, which extends down to nearly 0.1 Hz. BKS levels would be much higher if acoustic-to-elastic pRg conversion while transitioning across the oceanic/continental shelf boundary to shore was efficient.

[43] In contrast to similar SF and LPDF time histories, short-period DF (SPDF) signals in the [0.2, 0.3] Hz band at H2O and BKS (Figure 8e) appear unrelated, with the near-zero R^2 (Figure 8f, red line) consistent with the assessment that wave-wave interactions in the deep ocean do not generate DF microseism Rayleigh waves that are observed on continents. Also, because crustal body waves should not attenuate appreciably over the relatively short distance between H2O and BKS, the large difference in amplitude and lack of correlation between H2O and BKS in the SPDF band indicates that *P* wave microseism amplitudes in the SPDF band are much lower than pRg on the deep seafloor.

4.2. Mid-Ocean Extreme DF Events

[44] The highest amplitude DF signals observed at H2O during the 2001–2002 winter occurred during February and March 2002 in the [0.2, 0.3] Hz SPDF band (Figure 8a), characteristic of the oceanic DF peak (Figure 1). This band

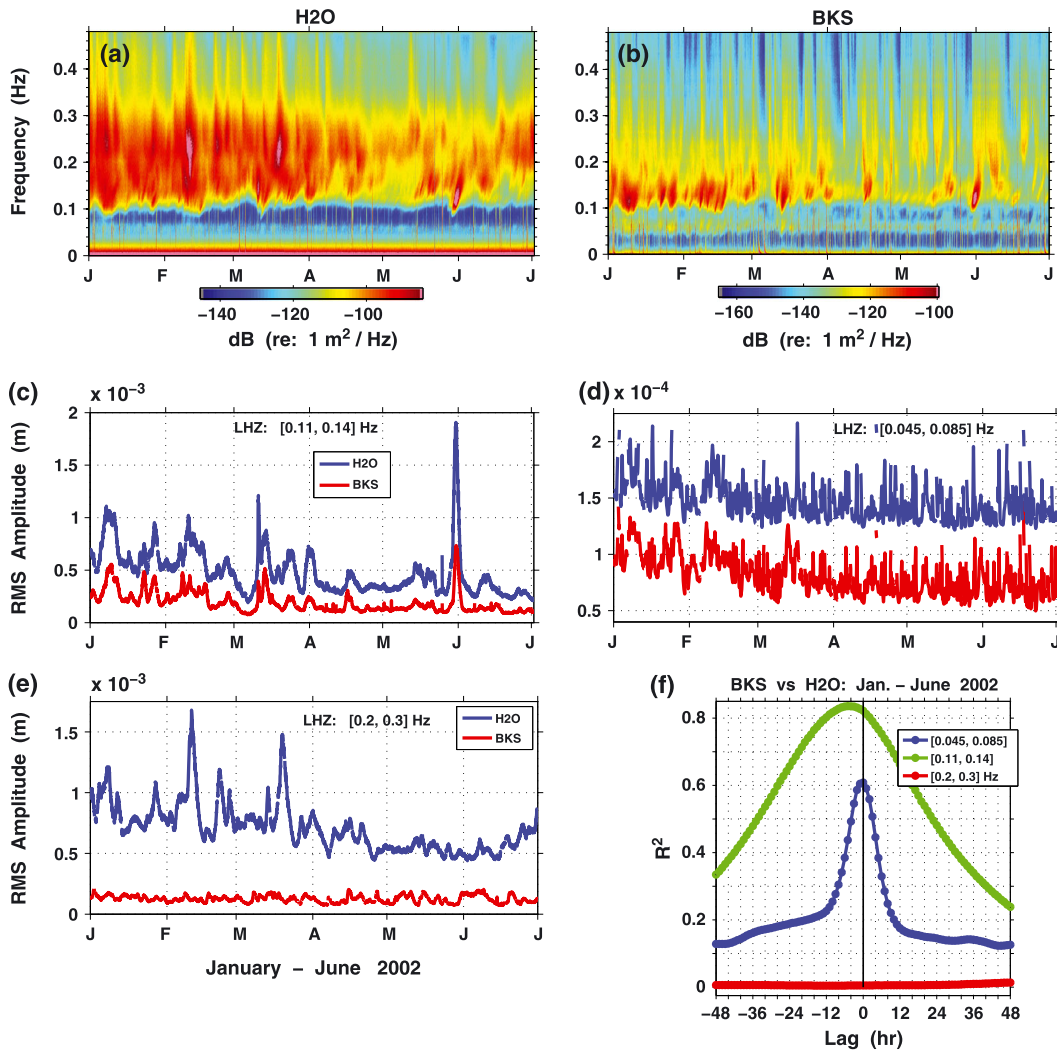


Figure 8. Relationships between (a) mid-ocean (H2O) and (b) coastal (BKS) microseism levels during January–June 2002. To allow identification of the highest amplitude signals, the upper bound in the amplitude range at H2O is 5 dB higher than at BKS. Root mean square (RMS) amplitudes of hourly averaged vertical component spectral levels at H2O (blue) and BKS (red) over (c) LPDF [0.11, 0.14] Hz, (d) primary microseism [0.045, 0.085] Hz, and (e) SPDF [0.2, 0.3] Hz frequency bands. (f) Correlation between the RMS amplitudes for the time series shown in Figures 8c–8e. Positive (negative) lags indicate signals at BKS lead (trail) H2O. Even though the longer-period SF signals attenuate less compared to DF, their relatively lower amplitudes result in stronger domination of locally generated DF signals at BKS, causing the much narrower correlation peak. The width of the lag-correlation peak is indicative of the amount of nonlocally generated DF energy, i.e., if all the DF signals were generated in one location, the lag-correlation function would be peaked at zero lag.

at times extends to lower frequencies, approaching 0.15 Hz, but we restrict the lower bound to 0.2 Hz in these analyses to avoid potential inclusion of LPDF energy in the SPDF comparisons. During 5–12 February 2002, multiple strong storm-forced wave events transited the North Pacific (see Supplement A2, *H_s* animation). Spectral levels above 0.3 Hz are generally associated with locally generated wind waves, either near-overhead in the case of H2O or at nearby coastal locations for BKS and WHY. Some of the high-amplitude DF signals at H2O near 0.25 Hz during 2–7 February likely were generated from wave activity associated with high waves in the open-ocean north of H2O (Figure 9a). Dispersed wave arrivals from this event reached the West Coast during 7–8 February, producing the SF/DF signals

observed at BKS. Only very strong coastal wave activity, such as on 10 February, produces distinct SF signals identified at H2O.

[45] The highest amplitude DF signals at H2O occurred on 10 February 2100 h (black dots Figures 9d–9f) when approximately 6 m waves occurred overhead. Examination of the wave model *H_s* animation (Supplement A2) suggests that initial wave activity northwest of H2O from this storm event produced the DF signals during 8–10 February in the [0.14, 0.2] Hz band (Figure 9d; the lack of prominent SF signals associated with these high-amplitude DF signals indicates a deep water source). Other wave activity at distant open-ocean locations (Figure 9b) potentially contributed to the extreme DF levels observed at H2O during 10–13 February. At the same time, high waves

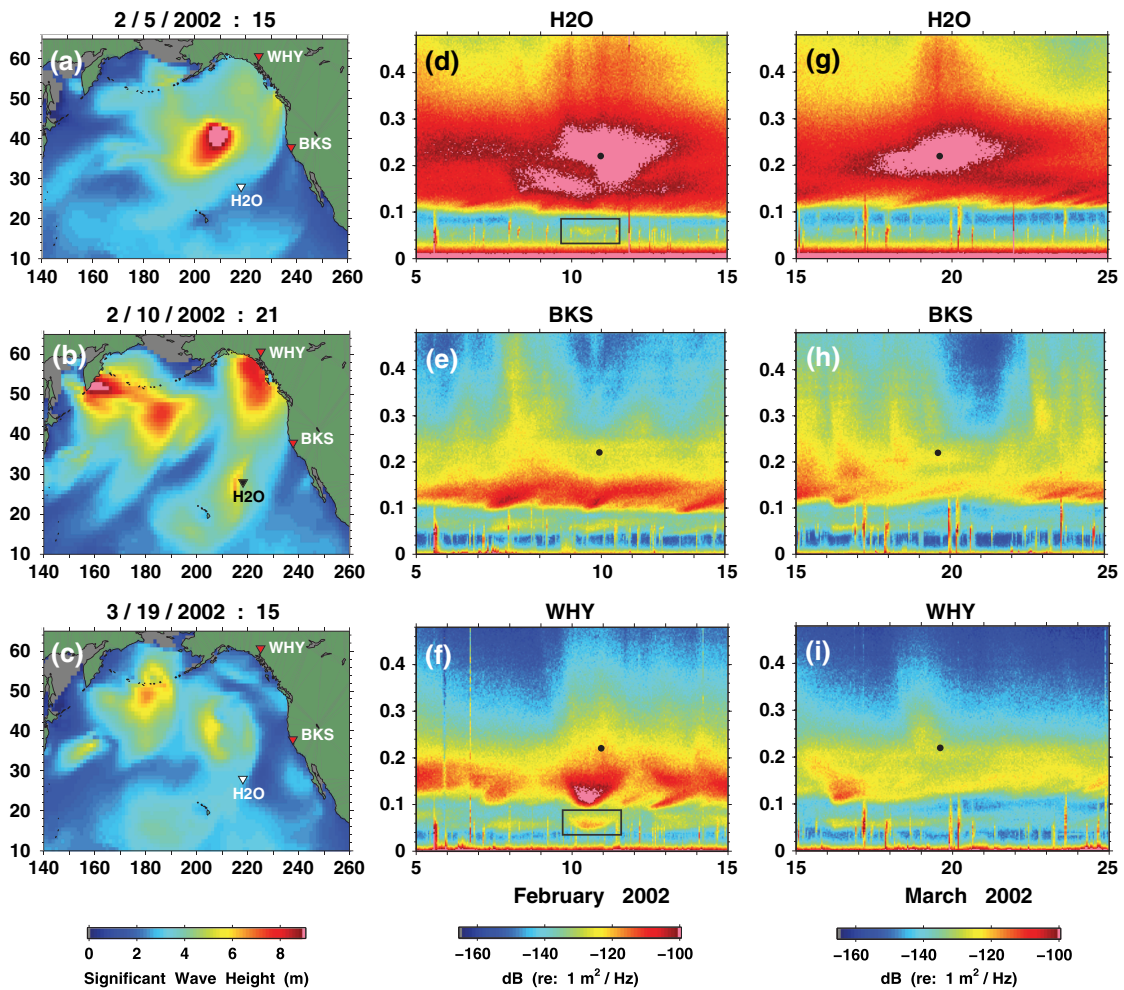


Figure 9. (a–c) WAVEWATCH III wave model significant wave height (H_s) snapshots during the 2002 winter over the North Pacific on (a) 5 February (b) 10 February, and (c) 19 March, time periods encompassing the highest amplitude DF microseism events recorded at mid-ocean bottom station H2O (see Figure 8). Vertical component displacement spectral levels recorded at H2O, BKS, and WHY, Whitehorse, Yukon Territory, Canada [60.6597°N, –134.8806°W, elevation 1292 m] during (d–f) 5–15 February, and (g–i) 15–25 March 2002, respectively. Vertical scale is frequency (Hz). Spectral scales shown apply to BKS and WHY. Note that H2O levels depicted span the [–160, –95] dB range, so that SF levels near 0.05 Hz at H2O on 10 February are close to those at WHY (boxed in Figures 9d and 9f), and DF level differences are actually more pronounced. The peak frequencies for these events at H2O (black dots in all spectrograms) are about 0.22 Hz for both February and March DF events (–83.86 and –86.33 dB levels, respectively). In comparison, the peak spectral level for the 30 May 2002 DF event studied by *Obrebski et al.* [2012] was near 0.12 Hz (–84.93 dB).

were impacting the Gulf of Alaska and Cascadia coasts, producing the SF (in black box) and DF signals observed at WHY (Figure 9f). The SF (primary) microseisms indicate that these signals were generated in shallow near-coastal water, and are most prominent at WHY, the coastal region where wave heights are greatest, and are clearly identified at H2O (Figure 9d, black box). The peak SF and DF near-coastal microseism levels at WHY from this event occur about a day prior to the strongest DF signals at H2O, when the wave amplitudes along the Cascadia coast were significantly greater than those shown on 10 February (Supplement A2). Waves from this event propagated southward along the coast, with gravity-wave dispersion producing the SF and DF spectral trends observed at BKS on 10–11 February (Figure 9e). DF energy generated near WHY also reached H2O and BKS, likely the

source of at least some of the DF energy near 0.12 Hz on 10 February, indicating that shallow water generated DF microseisms propagate seaward from near-coastal generation regions [*Bromirski et al.*, 2005]. However, the high-amplitude signals at H2O above 0.15 Hz on 12–13 February are not observed at either WHY or BKS (Figures 9e and 9f), where regional near-coastal wave activity can account for the DF signals observed. Beamforming and cross correlation of SCSN vertical component seismic data spanning this event detected no signals coming from a deep-ocean source region, consistent with findings of *Szelwis* [1982]. These observations demonstrate that, because the highest amplitude DF signals observed at H2O cannot be identified at continental stations, it is unlikely that any deep water-generated signals above 0.2 Hz can be detected on land.

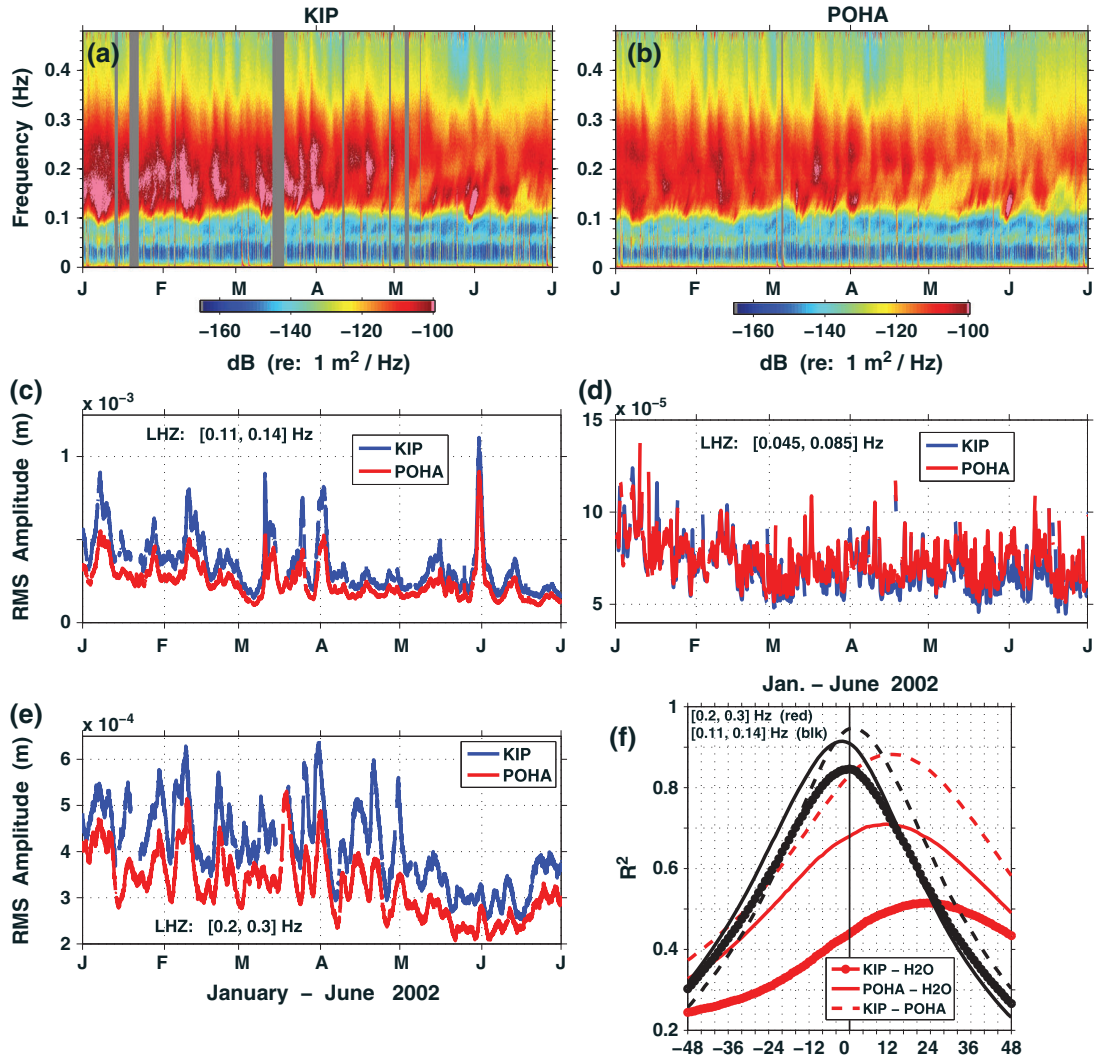


Figure 10. Relationships between microseism levels at seismic stations on (a) Oahu (KIP) and (b) the Big Island of Hawaii (POHA) with mid-ocean station H2O. Note that median spectral levels at KIP and POHA are about 5 dB lower than those at H2O (Figure 1). Root mean square (RMS) amplitudes of hourly averaged vertical component spectral levels at KIP (blue) and POHA (red) over (c) LPDF [0.11, 0.14] Hz, (d) SF microseism [0.045, 0.085] Hz, and (e) SPDF [0.2, 0.3] Hz frequency bands. (f) Correlation between the RMS amplitudes for the time series shown in Figures 10c and 10e, and with H2O. Correlation pairs for the SPDF band (legend, in red), apply to the LPDF band (black curves). Positive (negative) lags indicate signals at the first station identified leads (trails) the second.

[46] The wave model snapshot for 19 March 2002 (Figure 9c) shows low wave heights along the Pacific coast when an extreme DF event occurred at H2O (Figure 9g). It seems likely that deep-ocean wave interactions occurred during March 2002 northwest of H2O, producing the extreme DF levels at H2O during 18–21 March. At the same time, DF levels near the peak frequency at BKS and WHY (Figures 9h and 9i) were 30 dB lower and are likely generated by nearby near-coastal wave activity. Note the significant difference in the time histories of DF levels (particularly above 0.2 Hz) between H2O and the land stations during both the events. Although some ambiguity remains due to concurrent storm systems, the differences between H2O and the land stations are consistent with other observations showing that little, or no, deep-ocean-generated DF surface wave signals above 0.15 Hz are observed on land.

4.3. Mid-Ocean Versus Hawaiian Island Signal Comparisons

[47] DF microseism levels at island stations are known to be typically much higher than continental land stations (Figures 1 and 2) [Bromirski et al., 2005; Duennebier et al., 2012]. Elevated island DF levels may be due to (1) island stations being exposed to near-coastal wave activity generating DF microseisms from all directions, (2) some DF energy reaching island stations from the deep ocean. The patterns of spectral variability at Oahu (KIP) and the Big Island of Hawaii (POHA) (Figures 10a and 10b) are similar to those at H2O, and to a lesser extent BKS (Figures 8a and 8b). This suggests that propagation paths that do not traverse oceanic/continental crust boundaries may allow more deep water-generated DF energy to reach land stations. The spectral variability follows the pattern of storm wave variability

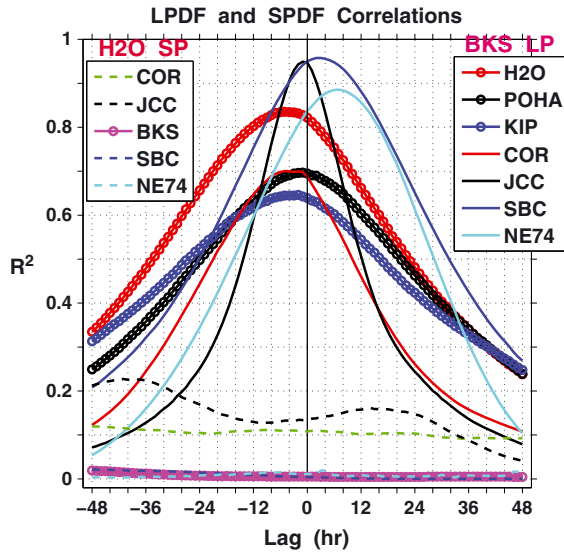


Figure 11. Relationship between coastal and mid-ocean microseism variability over January–June 2002. Lag-correlation curves of RMS vertical displacement spectral levels of long-period double-frequency (LPDF) microseism variability in the [0.11, 0.14] Hz band between coastal station BKS and other coastal and island stations. Also shown are lag correlations of RMS short-period double-frequency (SPDF) variability in the [0.2, 0.3] Hz band between mid-ocean station H2O with coastal stations (see Figures 3 and 4 for locations). COR is located in Corvallis, OR, about 100 km from the coast.

across the eastern North Pacific, with higher amplitudes during winter months (January–March) when storm activity is greater. Note that KIP levels are significantly higher than at POHA (separated by about 318 km), resulting from the more energetic wave climate at the northern Hawaiian Islands and/or a coastline configuration/orientation that is more conducive to producing opposing wave components.

[48] Both KIP and POHA have similar patterns of variability in both LPDF and SF bands (Figures 10c and 10d), with levels at KIP somewhat higher for LPDF. Because of the proximity of island stations to coasts, LPDF and SF microseisms are likely dominated by local near-coastal generation, although some contribution from the North American coast is likely [Bromirski *et al.*, 2005]. Not surprisingly, LPDF levels at KIP and POHA are well-correlated (Figure 10f, black dashed curve), with peak $R^2 > 0.9$. KIP slightly leads POHA, consistent with the initial arrival of stronger swell at more northern KIP dominating. DF signals propagating from northern Hawaiian Islands must contribute to DF observations at POHA. Similar to BKS, LPDF levels at KIP and POHA are well-correlated with H2O (Figure 10f, thick and thin black curves), with both island stations slightly leading H2O, consistent with dominant swell propagating from northwest to southeast. The somewhat higher LPDF R^2 between POHA and H2O as opposed to between KIP and POHA may result from the closer proximity of POHA to H2O, suggesting that either some of the LPDF energy reaching the Hawaiian Islands is generated by deep-ocean wave-wave interactions, or the wave climate near POHA and H2O is more similar than that between more distant and more northerly KIP and H2O. However, these correlations do not rule out the possibility that some of the LPDF signals at both island stations

have deep-ocean source contributions, although deep-ocean contributions are not necessary to explain the LPDF signal levels observed.

[49] In the SPDF band, KIP shows higher spectral levels (Figure 10e, blue curves), leads, and is well-correlated with POHA (Figure 10f, red dashed). These relationships are consistent with dominant storm and wave propagation from the northwest, first impacting Oahu and then dissipating somewhat while travelling down the Hawaiian Island chain. While local geology may be a factor (POHA is at 1990 m elevation on Mauna Kea and 10 km farther from coasts than KIP), the slightly longer propagation path would span less than one pRg wavelength and so would be unlikely to account for the large differences in spectral levels between KIP and POHA. In contrast to continental station BKS, both KIP and POHA show some SPDF correlation with H2O. KIP leads POHA, and both POHA and KIP lead H2O (Figure 8e, red curves). These relationships are also consistent with storm and wave propagation from the northwest, first exciting SPDFs at Hawaii and then over H2O. These observations demonstrate that deep-ocean to island DF signal propagation is not necessary to explain SPDF signal variability at the Hawaiian Islands.

5. Discussion

5.1. DF Propagation Across Ocean Crust

[50] Studies that attribute continental DF microseism observations to deep-ocean sources rest on the critical assumption that ocean wave interactions in the deep ocean generate seismic surface waves that propagate to the seafloor to land. For DF signals generated from deep-ocean sources, three propagation paths across oceanic crust are possible: (1) complete deep-ocean paths that are recorded by ocean bottom sensors, (2) deep-ocean paths that reach mid-ocean island stations, and (3) paths across ocean crust, through continental margins and on to continental stations. Additionally, two propagation paths are possible for DF signals generated in shallow near-coastal zones: (4) paths across oceanic crust to deep-ocean seafloor and island stations, and (5) the important path inland to continental stations.

[51] Virtually, all DF microseism studies recognize path (5) as viable. Paths (1) and (4) were identified by Bromirski *et al.* [2005] at H2O and pRg modes 0 and 1 have been observed on arrays of OBSs in the Pacific by Harmon *et al.* [2007] and Yao *et al.* [2011]. Observations of signals traversing path (2) were identified by Arduin *et al.* [2011] and Duennebier *et al.* [2012], although analyses presented here (section 4.2) are inconclusive. Path (3), the focus of this study, has been purportedly identified during particular events [Cessaro, 1994; Kedar *et al.*, 2008; Obrebski *et al.*, 2012, Stutzmann *et al.*, 2012]. However, most data, particularly [0.2, 0.3] Hz DF signals at H2O, indicate that path (3) rarely, if ever, occurs. Deep-ocean storm-generated DFs were observed at H2O but not on land [Bromirski *et al.*, 2005]. RMS amplitudes in the [0.2, 0.3] Hz SPDF band at H2O are poorly correlated with continental stations (Figure 11), consistent with little or no deep-ocean DF energy in this band reaching continents. Weak SPDF band correlations of H2O with COR and JCC more likely result from near-coastal wave interactions due to high intensity storm activity along the nearby coastlines than to common deep-ocean-generated DF signals. In contrast, the lower-frequency LPDF band energy at BKS is well correlated with H2O, and

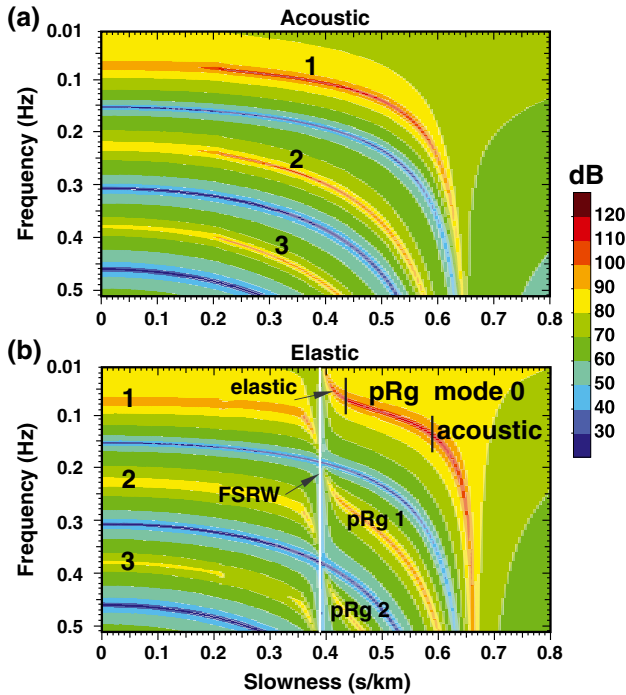


Figure 12. The magnitude of the wave fields in frequency-slowness space for a fluid layer (5 km thick with a sound speed of 1.520 km/s and a density of 1 kg/m³) over (a) a fluid half-space (acoustic (zero shear modulus), with sound speed of 4.730 km/s and density of 3 kg/m³), and (b) a solid half-space (elastic, compressional, and shear speeds of 4.730 and 2.800 km/s, respectively, FSRW wave speed of 2.565 km/s, and a density of 3 kg/m³). The FSRW slowness (0.39 s/km, white line) is the lower slowness bound for pseudo-Rayleigh wave (pRg) modes. Approximate boundaries where fundamental pRg mode 0 exhibits predominantly elastic or acoustic behavior are indicated by vertical black lines, with a transition region between. Acoustic modes 1, 2, and 3 are common to Figures 12a and 12b. Although the fluid half-space in Figure 12a is unrealistic, comparison of these cases shows the effect of shear. Source and receivers are 0.050 km above the interface. These plots were computed using a seismo-acoustic fast-field algorithm [Schmidt, 1988].

also with both other continental and island stations, indicating that DF energy from common events reaches all stations.

[52] Definitive studies by *Lacoss et al.* [1969] and *Haubrich and McCamy* [1969] using LASA land-based array data showed that the dominant seismic phase of microseisms detected by vertical seismometers varies with frequency: (a) at frequencies below 0.15 Hz, fundamental-mode Rayleigh waves (*Rg*) dominate; (b) from 0.15 to 0.3 Hz, microseisms are a combination of higher-order *Rg* and shear modes (*Lg*); (c) at frequencies higher than 0.15 Hz, the DF mechanism also produces body wave microseisms. Fundamental mode Love wave energy can be detected at low microseism frequencies by horizontal seismometers. These observations have been confirmed in later studies [Zhang et al., 2010; Brooks et al., 2009; Gerstoft et al., 2008; Tanimoto and Ishimaru, 2006]. Zhang and Lay [1995] and Kennett and Furumura [2002] have shown that *Lg* from earthquakes does not propagate efficiently through oceanic crust. As little as

100 km of ocean crust is sufficient to attenuate *Lg* below detectable levels. Therefore, the *Lg* microseisms observed at land stations could *not* be excited by storms over the deep ocean and thus must be generated nearshore. Also, although compressional body wave microseisms are observed by land seismic arrays, they are much weaker in amplitude than the *Lg* and *Rg* phases [e.g., Gerstoft and Tanimoto, 2007]. The crucial question we will address is whether pseudo-Rayleigh waves excited in the deep ocean propagate efficiently to land stations.

5.2. Solid Earth Seismology and Ocean Acoustics

[53] The physics of wave propagation over the 0.1–0.5 Hz frequency band for typical ocean depths (100–5500 m) spans the transition between solid earth seismology and ocean acoustics. The various types of seismic waves that propagate in a model consisting of a fluid layer over a homogeneous, solid half-space are well known: direct acoustic waves, compressional and shear head (body) waves, acoustic modes in the fluid layer, pseudo-Rayleigh waves (pRg), and Scholte waves [Roever et al., 1959; Strick, 1959a, 1959b; Ewing et al., 1957; Brekhovskikh, 1960; Biot, 1952; Cagniard, 1962; Scholte, 1948, 1949; Tolstoy, 1954; Bradley, 1994]. There are two general oceanic crustal cases: “soft” bottoms with shear speed less than the fluid sound speed, and “hard” bottoms where the shear speed is greater than the fluid sound speed. Because the acoustic wavelengths (λ , 3–15 km) at DF microseism frequencies are much longer than typical thicknesses of seafloor soft-sediment layers (<500 m), the seafloor sediments can, to first order, be ignored, and the bottom can be considered to consist of “hard” rock.

[54] The wave field for a water layer over a solid (elastic) hard-rock half-space differs significantly from the wave field over a fluid (acoustic) half-space (Figure 12). A 5000 m water layer over an acoustic bottom supports three modes in the microseism band (Figure 12a). Following convention, these are acoustic modes 1, 2, and 3 (from low to high frequency) [Jensen et al., 1994]. There is a cutoff frequency, at about 0.075 Hz, below which no acoustic modes are supported.

[55] Adding shear properties to the bottom (Figure 12b) introduces the pseudo-Rayleigh wave (pRg, with slownesses from 0.39 to 0.66 s/km), which does not have a cutoff frequency. This is the fundamental pRg mode, mode 0, and is the highest amplitude mode across the microseism band. It approaches the FSRW slowness (0.39 s/km) at low frequencies, and transitions from elastic pRg to a predominantly acoustic mode (with progressively increasing slowness) at higher frequencies (acoustic pRg). Two higher mode pRg branches (pRg modes 1 and 2) occur between 0.39 and 0.6 s/km slowness. The three pure-acoustic modes persist at slownesses below about 0.35 s/km. At some frequencies, both pure-acoustic and pRg modes are present, albeit with different slownesses. For example, at 0.25 Hz pure-acoustic mode 2, pRg mode 1, and the fundamental pRg mode 0 are all supported. In the limit as the water-layer thickness approaches zero, the only mode supported for a homogeneous, elastic half-space is the fundamental Rayleigh wave (mode 0), which is nondispersive and does not have a cutoff frequency. Note that because the model elastic half-space is homogeneous, *Lg* and “higher-order shear modes” due to layered crustal structure are not present in this example.

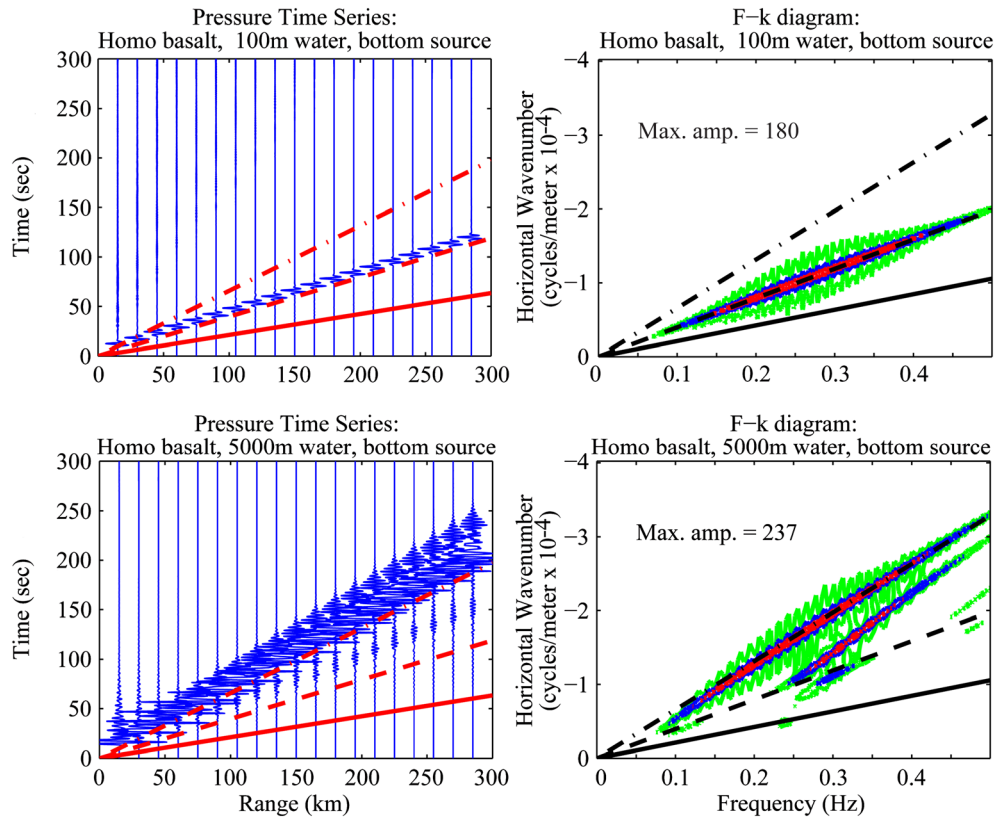


Figure 13. Time series (left) and the associated horizontal frequency-wave number response (right) from time domain finite difference model calculations for a point source in a shallow (100 m, top) and deep ocean (5000 m, bottom). The model consists of a homogeneous water layer over a homogeneous solid half-space. The compressional wave, shear wave, free-surface Rayleigh wave (FSRW), and acoustic wave speeds are 4730 (solid), 2740 (not shown), 2518 (dashed) and 1520 (dot-dashed) m/s. The frequency-wave number contours in Figures 13b and 13d are relative to the peak amplitude of each plot, with -10 dB (red), -20 dB (blue), and -30 dB (green).

5.3. Rayleigh Waves on Land and on the Seafloor

[56] It is important to distinguish whether the observations are made on land or on the seafloor, since simply saying “Rayleigh wave modes 0 and 1” is ambiguous and can lead to erroneous interpretations. The simplest land model is the free surface of a homogeneous solid half-space. In this model, the fundamental mode (mode 0) is nondispersive and travels at the FSRW speed (slightly less than the shear wave speed). For most crustal and mantle rocks, at the scale lengths appropriate for seismic waves at less than 1 Hz, the FSRW speed is substantially greater than 2 km/s. Higher-mode Rayleigh waves on land (e.g., mode 1) are supported by layered structure in the solid earth. On land, ambient noise studies rarely extract higher-mode Rg, requiring special structure and/or proximity to oceans [Brooks *et al.*, 2009; Yao *et al.*, 2011]. The simplest seafloor model consists of a homogeneous fluid layer over a homogeneous solid half-space. In this model, the fundamental mode (mode 0) is strongly dispersive through the microseism band (Figure 12). The phase speed varies from the FSRW speed to the water sound speed. Higher-mode pseudo-Rayleigh waves (modes 1, 2, ...) on the seafloor are supported by the water layer and exist even when the solid, subseafloor is homogeneous. Because of the strong water-layer influence, it would be remarkable “not” to observe higher-mode pseudo-Rayleigh waves in seafloor ambient noise studies. The shapes of the fundamental and

higher mode pRg dispersion curves, however, are strongly modified by layered subseafloor structure [Harmon *et al.*, 2007; Yao *et al.*, 2011].

[57] Observations using seafloor seismometers indicate that the fundamental pRg mode at 0.14 Hz (7 s period) is strongly attenuated with range across the deep water oceanic crust [Harmon *et al.*, 2007]. Harmon *et al.* determined that microseisms are primarily excited along coasts thousands of kilometers from their study area, with most of the energy concentrated in the water column (their Figure 9). These observations are consistent with LPDF microseisms identified in Figure 9 and by Bromirski *et al.* [2005]. Harmon *et al.* attributed a rapid falloff in pRg energy near 0.14 Hz to the loss of coherence caused by lateral variations in velocity. Because the energy at 0.14 Hz is concentrated in the water column, the velocity is highly sensitive to the water depth. Seamounts, volcanic ridges, and other oceanic crustal structures cause large local variations in velocity that both decrease coherence and increase scattering. Heterogeneous seafloor structure likely affects pRg propagation across all oceanic paths.

5.4. Excitation of Acoustic and Elastic Energy Versus Water Depth

[58] At microseism frequencies, typical ocean depths in λ span the range from thin (100 m water depth is $\lambda/30$ to $\lambda/150$) to near unity (5000 m water depth is 1.67 to 0.333 λ). The

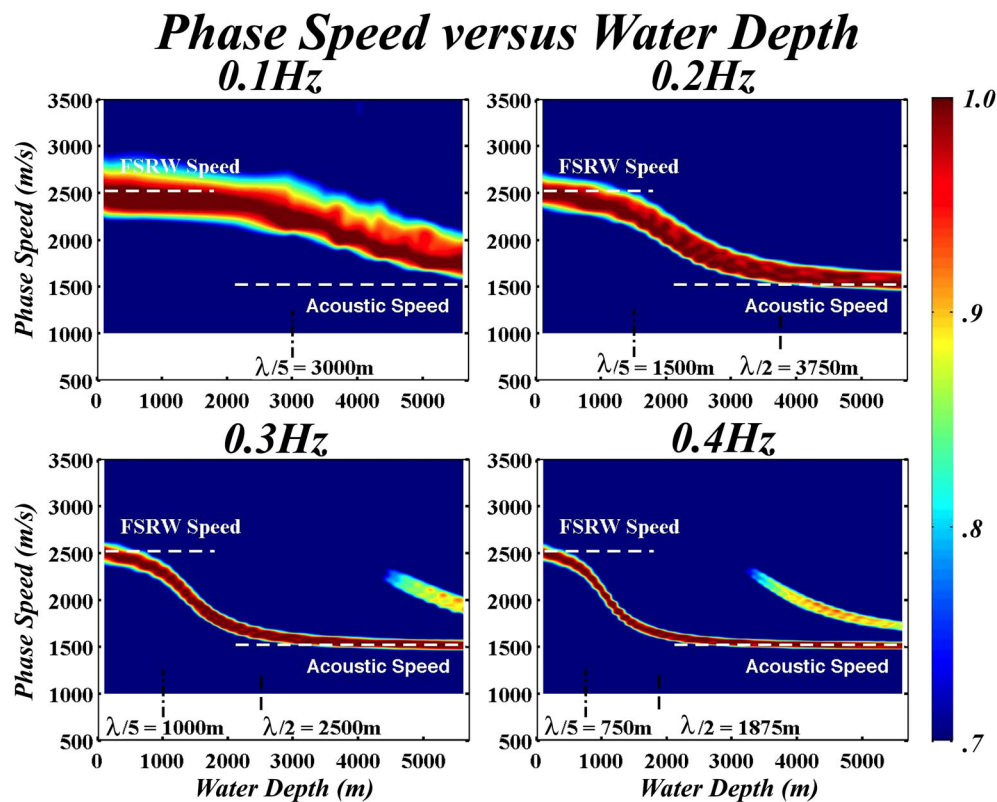


Figure 14. Relative wave field amplitude is shown as functions of phase speed and water depth for four frequencies (a) 0.1, (b) 0.2, (c) 0.3, and (d) 0.4 Hz. Spectral amplitudes (in dB) of the frequency-wave number field (as in Figures 13b and 13d) are averaged over a 0.2 Hz band about the nominal frequency, converted to phase speed and normalized to the peak amplitude on the trace. Acoustic sound speed (1520 m/s) and free-surface Rayleigh wave speed (FSRW, 2518 m/s) are indicated by horizontal dashed lines. The spectral peak variation shows that, for frequencies in the microseism band, the dominant energy transitions from FSRW speeds to acoustic speeds as water depth increases. Phase-speed resolution, indicated by the width of the spectral peak, improves with increasing frequency. pRg mode 1 (see Figure 12) becomes evident between FSRW and acoustic phase speeds at deeper water depths as frequency increases.

relative excitation of acoustic and elastic energy versus water depth was investigated with a series of two-dimensional time domain finite difference (Stephen [1988, 1990]; Stephen and Swift [1994]) models for water depths from 100 to 5000 m (Figures 13 and 14). The source spans the 0.1–0.5 Hz band, peaking at 0.25 Hz. The source is identical for all cases so that the relative strength of the arrivals can be compared across models. The source and receivers are 50 m ($< \lambda/60$) above the seafloor.

[59] Two types of plots are produced for each model in Figure 13: (1) time series showing the amplitude variability as a function of range and time, and (2) frequency-horizontal wave number (f-k) diagrams to compare the energy distribution of phases excited by the acoustic source. These demonstrate the significant differences in pRg excited in the microseism band due solely to the thickness of the water layer, with phase speeds indicative of either predominantly elastic pRg or acoustic pRg energy. For the 100 m water-depth case (Figure 13, top), the water is sufficiently thin with respect to any λ at the source frequencies that this is effectively a free-surface problem, resulting in most of the energy transformed into FSRW in the elastic bottom. The arrivals in the time series are the same shape as the source waveform (no dispersion) and move out at the FSRW phase speed (dashed lines). In shallow water, the ocean

layer is too thin to support much acoustic energy. This causes most of the source energy to be imparted into the solid half-space, elastic pRg, with the strength of the pressure field in the ocean quite weak.

[60] At 5000 m water depth (Figure 13, bottom), most of the source energy stays in the water layer as acoustic pRg and moves out at the water-wave speed (dot-dashed lines). Two dominant modes are observed (corresponding to the red bands in Figure 13d). The low-velocity (upper) mode conforms to the acoustic branch of pRg mode 0 and propagates at the water sound speed (1.52 km/s). (In contrast to the thin water-layer (FSRW) case, pRg mode 0 is strongly dispersive in the microseism band.) The higher velocity mode, with the steeper slope indicating a group speed less than the acoustic pRg speed but having a phase speed greater than the acoustic speed, is pRg mode 1 (refer to Figure 12b). Both of these modes have most of their energy in the fluid layer.

[61] The transition from elastic to acoustic pRg as a function of water depth is demonstrated for four frequencies spanning the microseism band (Figure 14). The relative wave field magnitude at four nominal microseism frequencies is plotted versus phase speed (a vertical trace on frequency-wave number plots in Figures 13b and 13d) and water depth. In shallow water, the dominant energy has a phase speed near the FSRW speed,

characteristic of elastic pRg waves. In deep water, the phase speed approaches the water sound speed, indicating acoustic pRg waves.

[62] Gravity-wave physics is well understood at the frequencies of interest, and if the amplitudes of the opposing waves are correct, the second-order wave-induced pressure will be well estimated in the deep ocean. However, there will always be some uncertainty in wind fields, so there will always be uncertainty in the waves. As discussed previously, the data indicate that most events observed at H₂O above 0.2 Hz result from deep water wave interactions. These are not detectable on continents (Figures 8 and 11). The co-occurrence of SF and DF microseisms for lower-frequency events (<0.15 Hz) with the same spectral time history argues for coastal generation being dominant, although at these lower frequencies, pRg phase speed-water depth relationships in Figure 14 indicate that deep water sources might contribute to the noise levels observed, assuming that losses from scattering under propagation and transitioning across the continental shelf boundary to the shore are not substantial. Much of the continental shelf and portions of the continental shelf boundary satisfy our shallow water criterion (<250 m) and could have been source areas during the *Obrebski et al.* event. However, if SF microseisms can be detected, it seems probable that near-coastal DF generation also occurs.

[63] As indicated by phase-speed relative-amplitude peak locations (Figure 14), acoustic sources in shallow water put most of their energy into the elastic pRg, but the same source in deep water puts the dominant portion of its energy into acoustic pRg. As frequency increases, acoustic pRg is excited at progressively shallower water depths. As the water layer thins, only elastic pRg can propagate efficiently. Because most of the pRg energy generated in shallow water propagates as an evanescent field in the solid (elastic pRg), it can transition from the deep ocean to land, and vice versa, at continental margins where the water-layer depth changes appreciably. Thus, wave interactions over shallow-water continental shelves excite predominantly elastic pRg that propagate easily into ocean basins and onto continents because they are supported by the rigidity of the solid earth. In general, elastic pRg wave behavior occurs at water depths less than 0.2λ , while acoustic pRg wave behavior occurs at water depths greater than 0.5λ . The intervening water depths are a transition region with mixed-mode behavior.

[64] Areas in the modeling that need to be better accounted for include propagation from deep water to land and shore reflection. There is uncertainty in: (1) how much opposing wave energy is present along coasts versus in the open ocean, (2) how much microseism energy in the deep ocean results from near-coastal wave activity that propagates into the ocean basins (not addressed in this paper or by *Obrebski et al.* [2012], *Ardhuin et al.* [2012], and others, but is seemingly significant, e.g., *Bromirski et al.* [2005]), (3) whether there are always DFs generated when waves reach the shore (the depth questions mentioned below), i.e., can there be primary microseisms without DF microseisms?, and (4) whether the full wave-wave interaction pressure field has been accounted for in shallow water. Currently, modeling of microseisms is based just on the 180° opposing wave-wave interaction. In deep water, this is fine. However, all components of the wave field interact, and this creates an important evanescent component in shallow water [*Cox and Jacobs*, 1989; *Bromirski and Duennebieber*,

2002]. This enhances shallow-water DF generation and would further add to the dominance of near-coastal wave activity generating the DF microseisms observed on land.

6. Conclusions

[65] Because high-amplitude waves from concurrent large storms potentially impact multiple coastal locations simultaneously, identification of deep-ocean sources is difficult. Without simultaneously measured ocean-wave and seismic spectra in the deep-ocean and at coastal locations near seismic stations, either deep-ocean or near-coastal sources can potentially explain the seismic observations. While wave interaction modeling is useful, it is not sufficient to confirm an open-ocean location using a single deep-ocean station and land-based data alone. Making multiple concurrent widely separated observations on the seafloor as well as on land are essential to resolve this issue. Because of these uncertainties and our investigation of ocean wave and microseism variability, we conclude that there is no unambiguous evidence that deep-ocean-generated microseisms are observed on land. Land seismic-array analyses have been unable to detect coherent microseism signals propagating from the deep ocean. Near-coastal shallow-water DF generation dominates land observations.

[66] Modeling indicates that elastic pseudo-Rayleigh wave (pRg) energy is not efficiently excited by acoustic sources in the deep (~5000 m) ocean, but is predominantly excited in shallow (<250 m) water. Recognizing that acoustic pRg does not propagate efficiently across deep-ocean/continental boundaries indicates that DF microseisms observed on land are primarily generated as fundamental elastic pRg by wave interaction in shallow near-coastal water. These constraints on DF source regions might improve imaging earth structure from surface wave tomography and are important considerations in reconstructing historical wave records using microseism data recorded at continental seismic stations.

[67] **Acknowledgments.** This work was supported by NSF grant OCE-1030022, the California Department of Boating and Waterways, NOAA grant NA10OAR4310121, and the Edward W. and Betty J. Scripps Chair for Excellence in Oceanography at WHOI (RAS). We thank IRIS DMC and the NCEC for providing seismic data, and NOAA NODC for providing buoy data, with hindcast data since 1992 obtained from <http://polar.ncep.noaa.gov>. Thanks to Paul Wittmann and John Helly for providing wave model *Hs* data prior to 1992.

References

- Aki, K., and P. G. Richards (2002), *Quantitative Seismology*, 2nd ed., 700 pp., University Science Books, Sausalito, CA.
- Ardhuin, F., and T. H. C. Herbers (2013), Double-frequency noise generation by surface gravity waves in finite depth: gravity, acoustic and seismic modes, *J. Fluid Mech.*, 716, 316–348, doi:10.1017/jfm.2012.548.
- Ardhuin, F., E. Stutzmann, M. Schimmel, and A. Mangeney (2011), Ocean wave sources of seismic noise, *J. Geophys. Res.*, 116, C09004, doi:10.1029/JC2011JC006952.
- Ardhuin, F., A. Balanche, E. Stutzmann, and M. Obrebski (2012), From seismic noise to ocean wave parameters: General methods and validation, *J. Geophys. Res.*, 117, C05002, doi:10.1029/2011JC007449.
- Babcock, J. M., B. A. Kirkendall, and J. A. Orcutt (1994), Relationships between ocean bottom noise and the environment, *Bull. Seismol. Soc. Am.*, 84(6), 1991–2007.
- Biot, M. A. (1952), The Interaction of Rayleigh and Stoneley waves in the ocean bottom, *Bull. Seismol. Soc. Am.*, 42, 81–93.
- Bradley, C. R. (1994), Very low frequency seismo-acoustic noise below the sea floor (0.2–10Hz), Ph.D. thesis, Massachusetts Institute of Technology and Woods Hole Oceanographic Institution.
- Bradner, H., and J. G. Dodds (1964), Comparative seismic noise on the ocean bottom and on land, *J. Geophys. Res.*, 69, 4339–4348.

- Brekhovskikh, L. M. (1960), Waves in Layered Media (Applied Mathematics and Mechanics, Vol. 6), 561 pp., *Translated from the Russian*, Academic Press, New York/London.
- Bromirski, P. D. (2001), Vibrations from the "Perfect Storm," *Geochem. Geophys. Geosyst.*, 2(7), 1030, doi:10.1029/2000GC000119.
- Bromirski, P. D., and F. K. Duennebieer (2002), The near-coastal microseism spectrum: Spatial and temporal wave climate relationships, *J. Geophys. Res.*, 107(B8), 2166, doi:10.1029/2001JB000265.
- Bromirski, P. D., R. E. Flick, and N. Graham (1999), Ocean wave height determined from inland seismometer data: Implications for investigating wave climate changes in the NE Pacific, *J. Geophys. Res. - C*, 104, 20,753–20,766.
- Bromirski, P. D., F. K. Duennebieer, and R. A. Stephen (2005), Mid-ocean microseisms, *Geochem. Geophys. Geosyst.*, 6, Q04009, doi:10.1029/2004GC000768.
- Bromirski, P. D., D. R. Cayan, N. Graham, R. E. Flick, M. Tyree (2012), Coastal Flooding-Potential Projections: 2000–2100, Scripps Institution of Oceanography, California Energy Commission, Publication number: CEC-500-2012-011, 54pp. ftp://ftp.iod.ucsd.edu/peter/Bromirski_etal_Coastal_Flooding_Potential_PIER_CVAS_2012.pdf.
- Brooks, L. A., J. Townend, P. Gerstoft, S. Bannister, and L. Carter (2009), Fundamental and higher-mode Rayleigh wave characteristics of ambient seismic noise in New Zealand, *Geophys. Res. Lett.*, 36, L23303, doi:10.1029/2009GL040434.
- Cagniard, L. (1962), *Reflection and Refraction of Progressive Seismic Waves*, 282 pp., McGraw-Hill, New York.
- Cao, S., and K. J. Muirhead (1993), Finite difference modeling of Lg blockage, *Geophys. J. Int.*, 116, 85–96.
- Cessaro, R. K. (1994), Sources of primary microseisms, *Bull. Seismol. Soc. Am.*, 84, 142–156.
- Cox, C. S., and D. C. Jacobs (1989), Cartesian diver observations of double frequency pressure fluctuations in the upper levels of the ocean, *Geophys. Res. Lett.*, 16, 807–810.
- Crawford, W. C., R. A. Stephen, and S. T. Bolmer (2006), A second look at low-frequency marine vertical seismometer data quality at the OSN-1 site off Hawaii for seafloor, buried, and borehole emplacements, *Bull. Seismol. Soc. Am.*, 96(5), doi:10.1785/0120050234.
- Duennebieer, F. K., R. Lukas, E.-M. Nosal, J. Aucan, and R. A. Weller (2012), Wind, waves, and acoustic background levels at Station ALOHA, *J. Geophys. Res.*, 117, C03017, doi:10.1029/2011JC007267.
- Elgar, S., T. H. C. Herbers, and R. T. Guza (1994), Reflection of ocean surface gravity waves from a natural beach, *J. Phys. Oceanogr.*, 24, 1503–1511.
- Ewing, W. M., W. S. Jardetzky, and F. Press (1957), *Elastic Waves in Layered Media*, 380 pp., McGraw-Hill, New York.
- Fukao, Y., K. Nishida, and N. Kobayashi (2010), Seafloor topography, ocean infragravity waves, and background Love and Rayleigh waves, *J. Geophys. Res.*, 115, B04302, doi:10.1029/2009JB006678.
- Gerstoft, P., and T. Tanimoto (2007), A year of microseisms in southern California, *Geophys. Res. Lett.*, 34, L20304, doi:10.1029/2007GL031091.
- Gerstoft, P., M. C. Fehler, and K. G. Sabra (2006), When Katrina hit California, *Geophys. Res. Lett.*, 33, L17308, doi:10.1029/2006GL027270.
- Gerstoft, P., P. M. Shearer, N. Harmon, J. Zhang (2008), Global P, PP, PKP wave microseisms observed from distant storms, *Geophys. Res. Lett.*, 35, L23306, doi:10.1029/2008GL036111.
- Harmon, N., D. Forsyth, and S. Webb (2007), Using ambient seismic noise to determine short-period velocities and shallow shear velocities in young oceanic crust, *Bull. Seismol. Soc. Am.*, 97, 2009–2023, doi:10.1785/0120070050.
- Hasselmann, K. (1963), A statistical analysis of the generation of microseisms, *Rev. Geophys.*, 1, 177–210.
- Haubrich, R. A., and K. McCamy (1969), Microseisms: Coastal and pelagic sources, *Rev. Geophys.*, 7, 539–571.
- Haubrich, R. A., W. F. Munk, and F. E. Snodgrass (1963), Comparative spectra of microseisms and swell, *Bull. Seismol. Soc. Am.*, 53(1), 27–37.
- Jensen, F. B., W. A. Kuperman, M. B. Porter, and H. Schmidt (1994), *Computational Ocean Acoustics*, 612 pp., American Institute of Physics, New York.
- Kalnay, E., et al. (1996), The NCEP/NCAR 40-year reanalysis project, *Bull. Seismol. Soc. Am.*, 77, 437–471.
- Kedar, S., M. S. Longuet-Higgins, F. H. Webb, N. Graham, R. W. Clayton, and C. E. Jones (2008), The origin of deep ocean microseisms in the North Atlantic Ocean, *Proc. R. Soc. A*, 464(2091), 777–793, doi:10.1098/rspa.2007.0277.
- Kennett, B. L. N. (1986), Lg waves and structural boundaries, *Bull. Seismol. Soc. Am.*, 76, 1133–1141.
- Kennett, B. L. N. (2001), *The Seismic Wavefield: Volume I, Introduction and Theoretical Development*, 380 pp., Cambridge University Press, Cambridge, U.K.
- Kennett, B. L. N., and T. Furumura (2002), Regional phases in continental and oceanic environments, *Geophys. J. Int.*, 146, 562–568.
- Lacoss, R. T., E. J. Kelly, and M. N. Toksoz (1969), Estimation of seismic noise structure using arrays, *Geophysics*, 34, 21–38.
- Latham, G. V., and G. H. Sutton (1966), Seismic measurements on the ocean floor, *J. Geophys. Res.*, 71, 2545–2573.
- Lin, F. C., M. H. Ritzwoller, N. M. Shapiro, and M. Nikolai (2006), Is ambient noise tomography across ocean basins possible? *Geophys. Res. Lett.*, 33, L4304, doi:10.1029/2006GL026610.
- Longuet-Higgins, M. S. (1950), A theory of the origin of microseisms, *Philos. Trans. R. Soc. Lond. A*, 243, 1–35.
- McCreery, C. S., F. K. Duennebieer, and G. H. Sutton (1993), Correlation of deep ocean noise (0.4–30 Hz) with wind, and the Holu Spectrum - A worldwide constant, *J. Acoust. Soc. Am.*, 93(5), 2639–2648.
- Obrebski, M. J., F. Ardhuin, E. Stutzmann, and M. Schimmel (2012), How moderate sea states can generate loud seismic noise in the deep ocean, *Geophys. Res. Lett.*, 39, L11601, doi:10.1029/2012GL051896.
- Okal, E. A. (1988), Seismic parameters controlling far-field tsunami amplitudes: A review, *Nat. Hazards*, 1, 67–96.
- Rhie, J., and B. Romanowicz (2006), A study of the relation between ocean storms and the Earth's hum, *Geochem. Geophys. Geosyst.*, 7, Q10004, doi:10.1029/2006GC001274.
- Roeber, W. L., T. F. Vining, and E. Strick (1959), Propagation of elastic wave motion from an impulsive source along a fluid/solid interface: I. Experimental pressure response, *Philos. Trans. R. Soc. Lond. A*, 251, 455–465.
- Schmidt, H. (1988), SAFARI, Seismo-Acoustic Fast Field Algorithm for Range-Independent Environments: User's Guide, SAACLANT Undersea Research Centre, 152 pp.
- Scholte, J. G. (1948), On the large displacements commonly regarded as caused by Love-waves and similar dispersive surface-waves, *Proc. K. Ned. Akad. Wet.*, 51, 533–543, 642–649, 828–835, 969–976.
- Scholte, J. G. (1949), On true and pseudo Rayleigh waves, *Proc. K. Ned. Akad. Wet.*, 52, 652–653.
- Schreiner, A. E., and L. M. Dorman (1990), Coherence lengths of seafloor noise: Effect of ocean bottom structure, *J. Acoust. Soc. Am.*, 88(3), 1503–1514.
- Schulte-Pelkum, V., P. S. Earle, and F. L. Vernon (2004), Strong directivity of ocean-generated seismic noise, *Geochem. Geophys. Geosyst.*, 5, Q03004, doi:10.1029/2003GC000520.
- Stephen, R. A. (1988), A review of finite difference methods for seismo-acoustics problems at the seafloor, *Rev. Geophys.*, 26, 445–458.
- Stephen, R. A. (1990), Solutions to range-dependent benchmark problems by the finite difference method, *J. Acoust. Soc. Am.*, 87, 1527–1534.
- Stephen, R. A., and S. A. Swift (1994), Modeling seafloor geoaoustic interaction with a numerical scattering chamber, *J. Acoust. Soc. Am.*, 96, 973–990.
- Strick, E. (1959a), Propagation of elastic wave motion from an impulsive source along a fluid/solid interface: II. Theoretical pressure response, *Philos. Trans. R. Soc. Lond. A*, 251, 465–488.
- Strick, E. (1959b), Propagation of elastic wave motion from an impulsive source along a fluid/solid interface: III. The pseudo-Rayleigh wave, *Philos. Trans. R. Soc. Lond. A*, 251, 488–523.
- Stutzmann, E., F. Ardhuin, M. Schimmel, A. Mangeney, and G. Tatau (2012), Modelling long-term seismic noise in various environments, *Geophys. J. Int.*, doi:10.1111/j.1365-246X.2012.05638.x.
- Szelwis, R. (1982), Modeling of microseismic surface wave source, *J. Geophys. Res.*, 87, 6906–6918.
- Tanimoto, T. (2007), Excitation of microseisms, *Geophys. Res. Lett.*, 34, L05308, doi:10.1029/2006GL029046.
- Tanimoto, T., and S. Ishimaru (2006), Seasonality in particle motion of microseisms, *Geophys. J. Int.*, 166, 253–266.
- Tolman, H. L. (2009), User manual and system documentation of WAVEWATCH III, version 3.14, Technical Note, U.S. Dept. of Commerce, NOAA, NWS, NCEP, Ocean Modeling Branch Contribution, 5200 Auth Road, Camp Springs, MD 20746.
- Tolstoy, I. (1954), Dispersive properties of a fluid overlying a semi-infinite elastic solid, *Bull. Seismol. Soc. Am.*, 44, 493–512.
- Traer, J., P. Gerstoft, P. D. Bromirski, W. S. Hodgkiss, and L. A. Brooks (2008), Shallow-water seismo-acoustic noise generated by tropical storms Ernesto and Florence, *J. Acoust. Soc. Am., Elec. Lett.*, doi:10.1121/1.2968296.
- Traer, J., P. Gerstoft, P. D. Bromirski, and P. Shearer (2012), Microseisms, infragravity waves, and hum from ocean surface gravity waves, *J. Geophys. Res.*, 117, B11307, doi:10.1029/2012JB009555.
- Wang, X. L., and V. R. Swail (2001), Changes of extreme wave heights in northern hemisphere oceans and related atmospheric circulation regimes, *J. Clim.*, 14, 2204–2221.
- Yao, H., P. Gouedard, J. A. Collins, J. J. McGuire, and R. D. van der Hilst (2011), Structure of young East Pacific Rise lithosphere from ambient noise correlation analysis of fundamental- and higher-mode Scholte-Rayleigh waves, *C. R. Geosci.*, 343, 571–583.
- Zhang, T.-R., and T. Lay (1995), Why the Lg phase does not traverse oceanic crust, *Bull. Seismol. Soc. Am.*, 85, 1665–1678.
- Zhang, J., P. Gerstoft, and P. D. Bromirski (2010), Pelagic and coastal sources of P-wave microseisms: Generation under tropical cyclones, *Geophys. Res. Lett.*, 37, L15301, doi:10.1029/2010GL044288.